The Two- to Four-Day Predictability of Midlatitude Cyclones: Don't Sweat the Small Stuff

DANIEL J. LLOVERAS,[a] DALE R. DURRAN,[a] AND JAMES D. DOYLE[b]

[a] *Department of Atmospheric Sciences, University of Washington, Seattle, Washington*
[b] *Naval Research Laboratory, Monterey, California*

(Manuscript received 15 November 2022, in final form 16 August 2023, accepted 17 August 2023)

ABSTRACT: We use convection-permitting idealized simulations of moist midlatitude cyclones to compare the growth of synoptic-scale perturbations derived from an adjoint model with the growth of equal-energy-norm, monochromatic-wavelength perturbations at the smallest resolved scale. For initial magnitudes comparable to those of initial-condition uncertainties in present-day data assimilation systems, the adjoint perturbations produce a "forecast bust," significantly changing the intensity and location of the cyclone and its accompanying precipitation. In contrast, the small-scale-wave perturbations project strongly onto the moist convection, but the upscale growth from the random displacement of individual convective cells does not significantly alter the cyclone's development nor its accompanying precipitation through 2–4-day lead times. Instead, the differences in convection generated at early times become negligible because the development of subsequent convection is driven by the mostly unchanged synoptic-scale flow. Reducing the perturbation magnitudes by factors of 10 and 100 demonstrates that nonlinear dynamics play an important role in the displacement of the cyclone by the full-magnitude adjoint perturbations, and that the upscale growth of small-magnitude, small-scale perturbations is too slow to significantly change the cyclone. These results suggest that a sensitive dependence on the synoptic-scale initial conditions, analogous to that of the Lorenz (1963) system, may be more relevant to 2–4-day midlatitude-cyclone forecast busts than the upscale error growth in the Lorenz (1969) model.

KEYWORDS: Extratropical cyclones; Synoptic-scale processes; Mesoscale processes; Baroclinic models; Numerical weather prediction/forecasting

1. Introduction

A fundamental challenge in the study of atmospheric predictability is to characterize how initial-condition errors grow as a function of their scale, structure, and magnitude. The foundational contribution to this problem was provided by Lorenz (1969), who introduced the idea that the atmosphere has a finite predictability limit owing to the upscale cascade of unobservable small-magnitude initial-condition errors. Lorenz showed that equal-absolute-magnitude initial-condition errors ultimately produce a loss of predictability on all spatial scales independent of their initial scale. The obvious impossibility of accurately observing the complete state of the atmosphere down to very small spatial scales led to a focus on difficulties arising from small-scale errors, as exemplified by the notion that the flapping of seagull, or even butterfly, wings could influence the entire global circulation over a period of a couple weeks.

Nevertheless, initial-condition errors on small spatial scales may have limited potential to influence the accuracy of forecasts for synoptic-scale systems. Tribbia and Baumhefner (2004) examined the growth of random initial-condition errors in a global model and concluded that "the prediction of synoptic and larger scales does not suffer exorbitantly from inaccurate specification of small scales." Durran and Gingrich (2014) revisited the Lorenz (1969) model, redimensionalizing it so that the background kinetic energy (KE) spectrum matched observations at a horizontal wavelength of 400 km. They showed that if similar relative errors are initially present at all scales, eliminating the errors at wavelengths less than 400 km has almost no influence on the error growth after the first few hours, whereas eliminating the initial errors at wavelengths longer than 400 km dramatically slows down the error growth.

Lorenz (1969) modeled homogeneous isotropic turbulence, but many of the most impactful limitations to atmospheric predictability involve errors in forecasts of coherent, isolated structures such as midlatitude cyclones. The extent to which small-scale motions meaningfully interact with such larger-scale features is not well established. The most widely cited paradigm for such interaction involves the three-stage conceptual model of Zhang et al. (2007) in which 1) errors initially "grow from small-scale convective instability," 2) those errors transform "to larger-scale balanced motions through geostrophic adjustment," and 3) the balanced components of the errors "grow with the background baroclinic instability."

Yet at the end of their 1.5-day simulation on a 10-km nested grid, Zhang et al. (2007, Fig. 11) found that the maximum large-scale (filtered) pressure difference that developed at 500 hPa in response to 0.2-K-standard-deviation Gaussian-noise perturbations to the potential temperature field was only 0.7 hPa, corresponding to about 10 m of height difference at 500 hPa. In simulations of a summertime convective event over Europe, Selz and Craig (2015, Fig. 7) found that 0.01-K-standard-deviation Gaussian-noise perturbations at the scale of their 2.8-km grid produced maximum large-scale perturbations in 500-hPa height of just 5 m after 2.5 days. In the context of

---

Corresponding author: Daniel J. Lloveras, lloveras@uw.edu

DOI: 10.1175/JAS-D-22-0232.1

real-world forecast busts over Europe, Rodwell et al. (2013, Fig. 9c) found that $O(10)$-m perturbations in a region over the Rocky Mountains were key perturbations, relative to the control, in the best ensemble member for a 6-day forecast. That is, the final perturbations obtained after 1.5 days by Zhang et al. (2007) were about the magnitude of the initial-condition perturbations required to correct a forecast bust developing after 6 additional days in the study by Rodwell et al. (2013). Another indication of how long it may take convectively generated errors to influence the synoptic-scale flow was provided by Baumgart et al. (2019, Figs. 5a,b). They found that the differences in the location of the dynamic tropopause (among five ensemble members driven by different initial seedings of a stochastic convection scheme) were small after 5 days of simulation, but became much more significant after 10 days.

The degree of convective instability in the cyclone environment might be expected to influence the rate at which small-scale initial-condition perturbations grow to influence the large-scale flow. Indeed, Tan et al. (2004) and Zhang et al. (2007) noted that decreasing the relative humidity in moist baroclinic-wave simulations diminishes the rate of error growth from small scales. Nevertheless, the environmental convective available potential energy (CAPE) in the southern part of the domain for their control simulations rises to unrealistic values of 6000 J kg^{-1}, and the clouds and vertical motions in their simulations are not characteristic of prototypical midlatitude cyclones (Lloveras et al. 2022, Fig. 4). One example of how small-scale perturbations might be expected interact with deep convection to influence larger scales in a more realistic highly convective environment was provided by Judt et al. (2016). They found that perturbations introduced through convective-scale stochastic KE backscatter had almost no influence on the ensemble spread in the track of Hurricane Earl over a 7-day forecast. Those perturbations did, however, generate spread in intensity after about 36 h.

Recent research has attempted to quantify the gap between "intrinsic" and "practical" predictability, and to estimate the improvement that could be achieved with a perfect model and data assimilation system (Zhang et al. 2019; Selz et al. 2022). Lorenz (1969) suggested that the atmosphere possesses "an intrinsic range of predictability which cannot be lengthened by reducing the error of the observation to any value greater than zero." Lorenz assumed that predictability was lost at a given horizontal scale when the KE of the forecast errors saturates as it reaches the same magnitude as the background KE spectrum at the same scale. In contrast to the idealized model for homogeneous isotropic turbulence seeded by random errors studied by Lorenz (1969), Zhang et al. (2019) and Selz et al. (2022) employed modern global atmospheric forecast models to investigate error growth in ensembles with initial-condition spread determined by state-of-the-art data assimilation systems. By rescaling initial ensemble perturbations to 10% (or even as little as 0.1%) of their original operational magnitude and examining the change in error growth rates, both of these studies estimated the gap between the intrinsic predictability of atmospheric motions and the performance of current forecast systems, concluding there is potential for extending the predictability of current midlatitude forecasts by 4–5 days. Similar to Lorenz (1969), the primary metric for determining loss of predictability in these studies was the saturation of the ensemble-spread KE, averaged over the midlatitudes and over many forecast cycles. As a consequence, these studies are not well suited to investigate individual low-predictability events, since these events are characterized by very large localized errors whose importance can be diluted in long-term averages over broad regions.

The goal of this paper is to examine initial-condition-error growth in a prototypical midlatitude cyclogenesis event. Many prior studies have used adjoint models to explore initial-condition sensitivities in midlatitude cyclones and found that the optimal perturbation structures for producing the fastest growth are on the synoptic and larger mesoscales (Langland et al. 1995, 1996, 2002; Doyle et al. 2014, 2019). Hindcast simulations in Doyle et al. (2014), for example, showed that both positive and negative adjoint-optimal perturbations with magnitudes characteristic of current analysis errors can create large differences in the position and intensity of the rapidly intensifying Cyclone Xynthia over 36-h periods. The relative importance of large- and small-scale initial-condition errors in simulations of an idealized midlatitude cyclone was specifically addressed by Sun and Zhang (2016). They found that error growth was dominated by wavelengths less than 200 km when the initial-error magnitude was very small, but "if the initial perturbation is sufficiently large in scale and amplitude (as for most current-day operational models), the baroclinic growth of large-scale finite-amplitude initial error will control the forecast accuracy." Their large-scale alternative to small-scale random noise was the fastest growing baroclinic mode in their periodic channel flow, filtered to retain wavelengths greater than 1000 km. They did not consider adjoint perturbations and did not normalize the initial difference KE of their large- and small-scale perturbations to be the same magnitude. In addition, as in Zhang et al. (2007), their idealized moist midlatitude cyclone deviates in many respects from a prototypical midlatitude system.

To more precisely compare the role of large- and small-scale initial-condition perturbations in a high-impact, synoptic-scale forecast problem, we directly compare the growth of equal-energy-norm small- and large-scale perturbations in realistic convection-permitting simulations of moist baroclinically unstable waves. We specify the small-scale perturbations to project onto regions of active precipitation in the developing cyclone, while we determine the large-scale perturbations using an adjoint model. We particularly focus on the perturbations required to significantly change the position and intensity of the low pressure center and generate a "forecast bust" at lead times of 2–4 days. We do not employ a rigorous definition of a bust like that of Rodwell et al. (2013), since we are not parsing through real-world forecasts to identify those with unusually low skill.

We describe the experimental design, including details about the numerical model and the initial-condition perturbations, in section 2. We discuss the changes to the cyclone produced by the perturbations in section 3. We consider the error-growth dynamics, including the adjustment of the synoptic-scale errors toward geostrophic balance, in section 4. We compare the impact of initial-condition perturbations

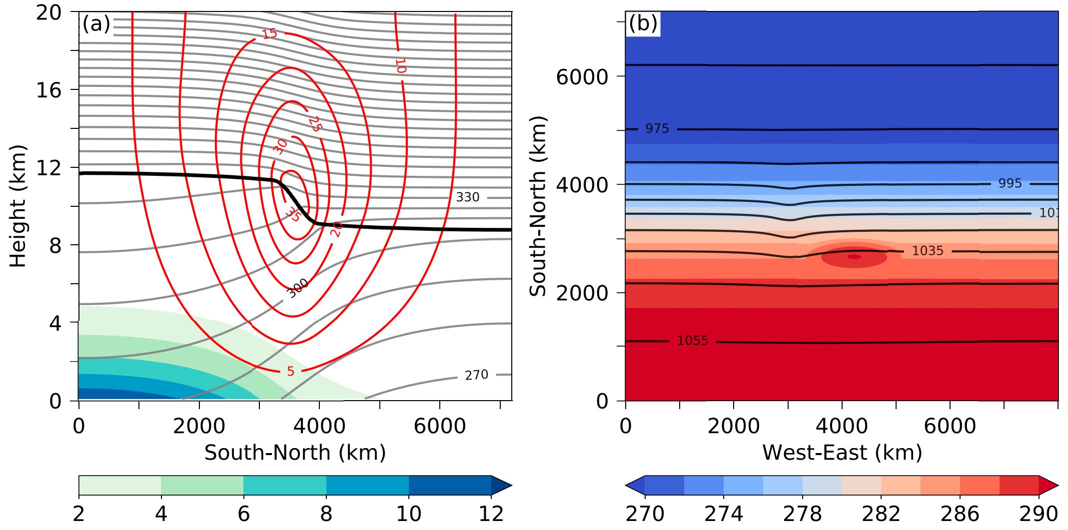

FIG. 1. (a) South–north vertical cross section of the background-state zonal wind (red contours every 5 m s^{-1}), potential temperature (gray contours every 10 K), and water vapor mixing ratio (color fill every 2 g kg^{-1}). The 1.5-PVU black line indicates the tropopause. (b) Initial surface potential temperature (color fill every 2 K) and 250-hPa geopotential height (black contours every 10 dam).

added at different times during cyclogenesis in section 5. We provide our conclusions in section 6.

2. Experimental design

a. Model configuration

We use the Advanced Research version of the Weather Research and Forecasting Model (WRF-ARW version 3.6.1; Skamarock et al. 2008) to run simulations of idealized midlatitude cyclones developing in moist baroclinically unstable *f*-plane channels with zonally periodic and meridionally symmetric boundary conditions. This simulation setup is similar to that of previous studies investigating the predictability of moist baroclinic waves (Tan et al. 2004; Zhang et al. 2007; Sun and Zhang 2016), but we make three main changes to the simulations to improve their realism. First, we decrease the convection-permitting grid spacing from 10 to 4 km to better represent error growth from moist convection. Second, we decrease the domain-maximum CAPE from the highly unrealistic 6000 J kg^{-1} to a more reasonable 500 J kg^{-1}. Third, the procedure for generating the zonally uniform background state (Fig. 1a) follows that of the constant tropospheric static stability (CTSS) simulations in Lloveras et al. (2022, section 2), which contains a detailed discussion on how the CTSS environment is superior for producing realistic vertical motions in the presence of moisture. Note that, while we use the formulas in the appendices of Lloveras et al. (2022) to generate the background state, we alter the values of some of the parameters to produce a sharper increase in static stability along the tropopause and to keep the domain-maximum CAPE at 500 J kg^{-1}. The values of these parameters can be found in the Python code for creating the WRF input files for these simulations, which we include as part of the data availability statement.

The domain configurations and physics options are identical to those of the CTSS simulations in Lloveras et al. (2022). The zonal length is $L_x = 8000$ km, the meridional length is $L_y = 7200$ km, and there are 100 vertical levels with a model top at 20 km. We use the Yonsei University (YSU) planetary boundary layer scheme (Hong et al. 2006), the revised surface-layer scheme based on the Fifth-generation Pennsylvania State University–National Center for Atmospheric Research Mesoscale Model (MM5) parameterization (Jiménez et al. 2012) with the default roughness of $z_0 = 0.01$ m (there are fluxes of momentum, but fluxes of heat and moisture are set to zero), the National Severe Storms Laboratory (NSSL) two-moment microphysics scheme (Mansell et al. 2010), and the Rayleigh damping scheme from Klemp et al. (2008) in the top 5 km of the model. We do not include solar nor infrared radiation, and we do not use cumulus parameterization.

In Lloveras et al. (2022), an ellipsoidal PV anomaly located in the middle troposphere triggered the development of a realistic midlatitude cyclone. However, PV anomalies associated with midlatitude cyclogenesis do not typically originate in the middle troposphere. Instead, they are found near the tropopause as an extrusion from the high-PV stratosphere or in the lower troposphere due to diabatic processes like latent heat release (Davis and Emanuel 1991; Brennan et al. 2008; Crezee et al. 2017). Thus, for the simulations presented here we use two anomalies to trigger cyclogenesis: a PV anomaly situated at the tropopause, and a surface thermal anomaly that leads to a local tightening of the surface temperature gradient. Consistent with observations of precursor disturbances for cyclogenesis (Hakim 2000), the localized tropopause and surface anomalies have horizontal radii $O(500)$ km, but are elliptical rather than circular to represent an upper-level PV streamer and a surface frontal zone, respectively. We use piecewise quasigeostrophic PV (QGPV) inversion (Hakim et al. 1996)

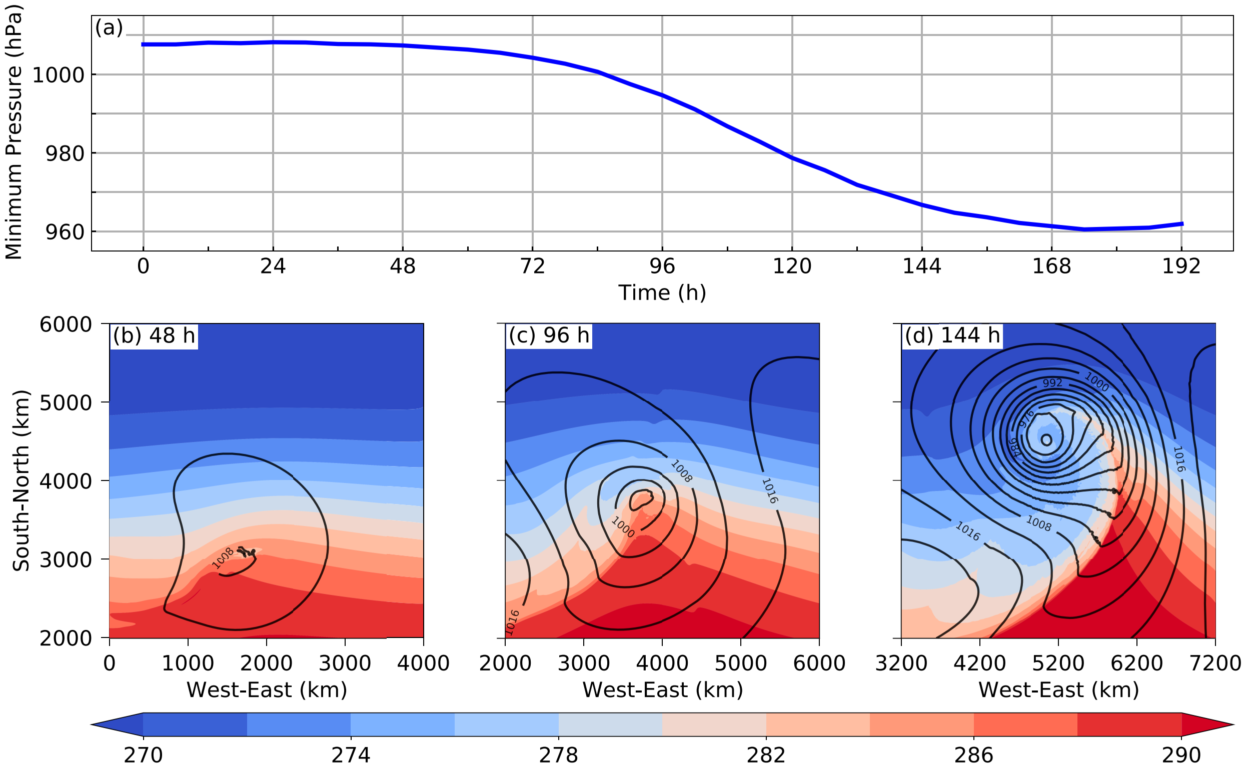

FIG. 2. (a) Time series of minimum surface pressure for the control simulation. (b)–(d) Surface pressure (black contours every 4 hPa) and surface potential temperature (color fill every 2 K) for the control simulation at (b) 48, (c) 96, and (d) 144 h.

to obtain the zonal and meridional wind, potential temperature, and pressure fields corresponding to the superposition of the two PV anomalies.

The tropopause anomaly is of the form

$$Q'(x, y, z) = Q_0 \cos r_{\mathrm{ht}} \cos r_z, \qquad (1)$$

where $Q_0 = 10^{-4}\ \mathrm{s}^{-1}$, $r_{\mathrm{ht}} = \sqrt{[(x - x_{\mathrm{ct}})/\delta_{\mathrm{xt}}]^2 + [(y - y_{\mathrm{ct}})/\delta_{\mathrm{yt}}]^2}$, and $r_z = |(z - z_c)/\delta_z|$. The horizontal decay scales are $\delta_{\mathrm{xt}} = 200$ km and $\delta_{\mathrm{yt}} = 600$ km and the vertical decay scale is $\delta_z = 1.5$ km. The parameters r_{ht} and r_z are capped at $\pi/2$. The center of the anomaly is at $(x_{\mathrm{ct}}, y_{\mathrm{ct}}, z_c) = (3000\ \mathrm{km}, 3600\ \mathrm{km}, 10\ \mathrm{km})$.

The surface anomaly is generated by solving the QGPV equation for zero internal PV and imposing a boundary condition for potential temperature of the form

$$\theta'_s(x, y) = \theta_0 \cos r_{\mathrm{hs}}, \qquad (2)$$

where $\theta_0 = 5$ K and $r_{\mathrm{hs}} = \sqrt{[(x - x_{\mathrm{cs}})/\delta_{\mathrm{xs}}]^2 + [(y - y_{\mathrm{cs}})/\delta_{\mathrm{ys}}]^2}$, with r_{hs} capped at $\pi/2$. The decay scales are $\delta_{\mathrm{xs}} = 600$ km and $\delta_{\mathrm{ys}} = 200$ km and the center of the anomaly is at $(x_{\mathrm{cs}}, y_{\mathrm{cs}}) = (4200\ \mathrm{km}, 2700\ \mathrm{km})$, placing it to the southeast of the tropopause PV anomaly. The boundary thermal anomaly can be interpreted as a spike of positive PV at the surface following Hoskins et al. (1985) and yields a cyclonic circulation when inverted.

Figure 1b shows the relative positions of the surface and tropopause PV anomalies. The tropopause anomaly leads to an upper-level trough oriented to the west of the tightened surface temperature gradient, which is a favorable orientation for mutual amplification of the PV anomalies. Note that for visualization purposes, from this point forward we roll the data by 4000 km in the zonal direction so that the developing cyclone does not straddle the periodic boundary.

Figure 2 shows the evolution of the cyclone produced by the interaction of the two PV anomalies. For the purposes of our predictability experiments, we refer to this simulation as the "control," as it does not contain any of the perturbations used to investigate error growth. The time series of minimum surface pressure (Fig. 2a) shows that the cyclone begins to deepen just before 48 h into the simulation. The beginning of the cyclone's development is characterized by a sharp cold front along the pressure trough (Figs. 2b,c). The fastest deepening occurs between 96 and 120 h, with the central pressure decreasing by about 15 hPa over this 24-h period. The deepening rate begins to decrease after 120 h, with an occluded front forming by 144 h (Fig. 2d). The cyclone reaches its lowest pressure of 960 hPa after about a week of development.

In this study, we conduct "identical-twin" predictability experiments in which we add perturbations to the simulation at a given time and contrast the subsequent development with that of the unperturbed control simulation. In this way, the perturbations can be viewed as "initial-condition errors" and the differences between the perturbed and control simulations can be viewed as "forecast errors." Our goal is to contrast the growth of synoptic-scale initial-condition errors with the growth of monochromatic-wavelength initial-condition errors at the smallest resolved scale. Our main focus is on a set of experiments in which we add these perturbations at 48 h into the control simulation (Fig. 2b). At this time, the control cyclone is just beginning to deepen, and there is sufficient precipitation to produce error growth via moist processes. We refer to the time after perturbations are added as the "forecast lead time." For example, if we add the perturbations at 48 h and then examine the simulation at 96 h, we are examining the forecast at a lead time of 48 h. In section 5 we consider error growth when perturbations are added at later stages of the cyclone's development.

b. *Adjoint-derived perturbations*

We derive synoptic-scale perturbations using an adjoint model. Ideally we would use the adjoint model for WRF (Zhang et al. 2013), but the code is built within WRF's four-dimensional variational data assimilation module, so there is no user interface for stand-alone adjoint runs. Instead, we use the adjoint of the atmospheric module of the Coupled Ocean–Atmosphere Mesoscale Prediction System (COAMPS; Amerault et al. 2008; Doyle et al. 2012) closely following the configurations of Doyle et al. (2014, 2019). The COAMPS tangent-linear and adjoint models include the nonhydrostatic dynamical core and parameterizations for the planetary boundary layer (using a 1.5-order closure for turbulent kinetic energy), surface-layer, cumulus, and microphysics (using a 6-class scheme).

The procedure for computing the adjoint-derived perturbations follows that of Doyle et al. (2014, 2019). The adjoint model is used to describe the effect of the model state at the initial time $\mathbf{x}_{t_0}$ on a forecast metric J corresponding to the model state at the final time $\mathbf{x}_t$,

$$J(\mathbf{x}_t) = J[M(\mathbf{x}_{t_0})], \tag{3}$$

where M is the nonlinear model. Since midlatitude-cyclone forecasts often focus on the location and intensity of the low pressure center, here we define J as the average negative pressure perturbation in a 1 km layer above the region where the pressure at the lowest model level is less than 992 hPa. The adjoint sensitivity is the gradient of J with respect to the initial model state,

$$\frac{\partial J}{\partial \mathbf{x}_{t_0}} = \mathbf{M}^{\mathrm{T}} \frac{\partial J}{\partial \mathbf{x}_t}, \tag{4}$$

where $\mathbf{M}$ is the tangent-linear model of M and the adjoint model $\mathbf{M}^{\mathrm{T}}$ is formulated by taking the transpose of the tangent-linear model.

Changes to the response function J can then be expressed as

$$J' = \sum_{m,j} \frac{\partial J}{\partial x_{m,j}} x'_{m,j}, \tag{5}$$

where $\partial J/\partial x_{m,j}$ is the adjoint sensitivity gradient of the response function with respect to the initial value of variable m at grid point j. Following Doyle et al. (2014, 2019), the perturbations $x'_{m,j}$ are defined for each initial-state variable (zonal and meridional wind, pressure, potential temperature, and water vapor mixing ratio) as

$$x'_{m,j} = \frac{s}{w_m} \frac{\partial J}{\partial x_{m,j}}, \tag{6}$$

where the weights w_m are determined by the domain-maximum forecast differences for each variable m over a 24-h period,

$$w_m = [\max_j(|x^m_{t_{24}} - x^m_{t_0}|)]^{-2}. \tag{7}$$

The scaling parameter s is defined such that the largest perturbation for zonal wind, potential temperature, or water vapor does not exceed 1 m s^{-1}, 1 K, or 1 g kg^{-1}, respectively.

We run the adjoint simulations over 48-h time periods. This integration time period is common in the adjoint sensitivity analysis of real-world midlatitude cyclones (Doyle et al. 2019) and is comparable to the 36-h forecast periods analyzed in previous studies on the predictability of moist baroclinic waves (Tan et al. 2004; Zhang et al. 2007; Sun and Zhang 2016). For our main set of predictability experiments, the 48-h time period corresponds to 48–96 h in the control WRF simulation (Figs. 2b,c). In section 4c we evolve the perturbations to a longer lead time of 96 h, and in section 5 we consider adjoint runs at later stages of the cyclone's development.

To satisfy the tangent-linear approximation over the 48-h periods, the grid spacing for the adjoint runs is 32 km, which is much coarser than the 4-km grid spacing used in the WRF runs. Thus, we obtain the initial state for the adjoint runs in COAMPS by interpolating the 48-h WRF fields for zonal and meridional wind, pressure, potential temperature, and water vapor mixing ratio from 4- to 32-km grid spacing and from the WRF vertical coordinate to that of COAMPS. Once we obtain the perturbations $x'_{m,j}$ using the method described above, we interpolate these perturbations from the COAMPS grid with 32-km horizontal grid spacing onto the WRF grid with 4-km grid spacing for use in our predictability experiments. Note that the adjoint perturbations have a nearly identical impact on the nonlinear WRF run with 32-km grid spacing as they do on the nonlinear COAMPS run with 32-km grid spacing (not shown), which suggests that the sensitivity results are not strongly dependent on the model used.

Figures 3a and 3c show the horizontal and vertical structure, respectively, of the adjoint-derived potential-temperature perturbations added at 48 h into the control simulation. The maximum perturbation is 1 K because potential temperature is the variable that imposes the constraint on the scaling parameter s; notably, the wind perturbations are very small, with absolute maxima less than 0.15 m s^{-1}. The perturbations are on the order of 1000 km in horizontal scale, are maximized in the lower troposphere, and slope strongly upshear with height. These characteristics are similar to those found in studies that conducted adjoint-sensitivity analyses for real-world midlatitude cyclones (Ancell and Hakim 2007; Doyle et al. 2014, 2019) and for both dry and moist idealized cyclones (Langland et al. 1995, 1996).

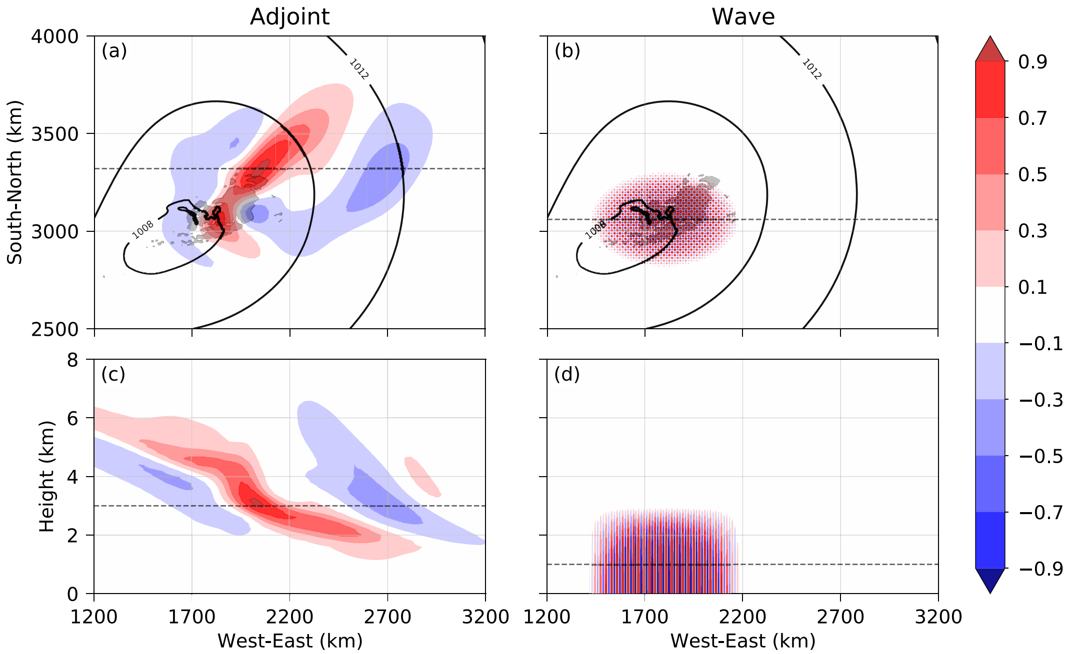

FIG. 3. (a),(c) Adjoint-derived potential-temperature perturbations (color fill every 0.2 K) at 48 h into the control simulation along (a) the x–y plane and (c) the x–z plane. In (a), the black contours denote the control surface pressure every 2 hPa, the gray shading indicates where the control modeled composite reflectivity exceeds 5 dBZ, and the dashed black line corresponds to the location of the cross section in (c). The dashed black line in (c) corresponds to the height of the potential-temperature perturbations in (a). (b),(d) As in (a) and (c), but for the small-scale-wave potential-temperature perturbations.

The maximum perturbation of 1 K is positive and flanked by much weaker negative perturbations on either side. The perturbations are oriented to the northeast of the low pressure center, and the largest-magnitude features are located away from the precipitating regions.

These adjoint perturbations are optimal in the sense that they produce the greatest change to the surface pressure response function as expressed by (5) for the smallest-magnitude perturbations subject to the constraint imposed by the scaling parameter s in (6). Although the adjoint model is limited by its tangent-linear approximation, this linearization is about a complex nonlinear trajectory rather than the zonally uniform background state. Thus, the adjoint is able to represent highly perturbed states (relative to the zonally uniform background) without violating the linearization hypothesis that the perturbations are small compared to the total fields in the unperturbed control simulation. In section 4c we provide a more detailed discussion of the role of nonlinearity in our experiments.

c. Small-scale-wave perturbations

To initiate error growth from small scales, we use surface-based, monochromatic-wavelength perturbations as in Lloveras et al. (2022), but to facilitate quantitative comparison with the adjoint perturbations, the small-scale waves are localized to a packet rather than distributed throughout the entire horizontal domain. Since we expect the small-scale-wave perturbations to grow primarily via moist processes, we design the packet to be roughly coincident with the main region of precipitation. The small-scale-wave potential-temperature perturbations are shown in Figs. 3b and 3d and are of the form

$$\theta'(x, y, z) = \begin{cases} \cos\left(\frac{\pi z}{2}\right)\sin\left(\frac{2\pi x}{L}\right)\sin\left(\frac{2\pi y}{L}\right)\cos r_{\mathrm{hp}}, & \text{if } z \le 3\text{ km}, \\ 0, & \text{if } z > 3\text{ km}, \end{cases} \quad (8)$$

where $r_{\mathrm{hp}} = \sqrt{[(x - x_{\mathrm{cp}})/\delta_{\mathrm{xp}}]^2 + [(y - y_{\mathrm{cp}})/\delta_{\mathrm{yp}}]^2}$. We place the horizontal center at $(x_{\mathrm{cp}}, y_{\mathrm{cp}}) = (1800\text{ km}, 3060\text{ km})$ and choose the decay scales of $(\delta_{\mathrm{xp}}, \delta_{\mathrm{yp}}) = (250\text{ km}, 160\text{ km})$. The monochromatic wavelength is $L = 28$ km, which is the smallest wavelength considered to be within the "effective" model resolution ($7\Delta x$; Skamarock 2004).

We also add these wave perturbations to the moisture and pressure fields. We compute the moisture perturbations using (8), but we scale the magnitude so that the ratio between the maximum perturbations for potential temperature and water vapor mixing ratio is equal to the ratio between the corresponding adjoint perturbations for those variables. The pressure perturbations are in hydrostatic balance with the potential-temperature perturbations. Recalling that the maximum-magnitude velocities are less than 0.15 m s^{-1} in the adjoint perturbations, we do not add wave perturbations to the zonal nor the meridional wind.

We scale the magnitude of the wave perturbations so that the domain-integrated difference total energy (DTE) matches

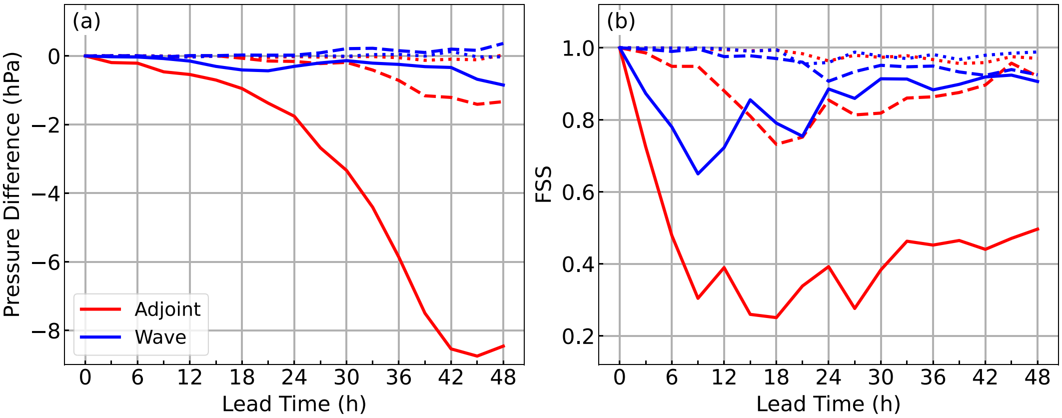

FIG. 4. Time series of (a) the differences in minimum surface pressure between the perturbed and control simulations and (b) the fractions skill scores (FSS) for precipitation through 48-h lead times for the experiments with the adjoint (red) and wave (blue) perturbations. The solid, dashed, and dotted lines correspond to the full-, 1/10-, and 1/100-magnitude experiments, respectively.

that of the adjoint perturbations. The DTE is the error metric used in Zhang et al. (2007) and is given by

$$\mathrm{DTE} = \frac{1}{2}[(\delta u)^2 + (\delta v)^2 + \kappa(\delta T)^2], \qquad (9)$$

where δu, δv, and δT are the differences between the perturbed and control fields of zonal wind, meridional wind, and temperature, respectively. The constant $\kappa = c_p/T_r$, where $c_p = 1004\ \mathrm{J\ K^{-1}\ kg^{-1}}$ is the specific heat at constant pressure and $T_r = 270$ K is a reference temperature.

Note that the potential-temperature and pressure perturbations are all that contribute to the DTE since there are no small-scale-wave perturbations to the wind fields. Because of this, and the fact that the perturbations are highly localized in the horizontal and shallow in the vertical, the maximum absolute value of the small-scale-wave potential-temperature perturbations is about twice that of the adjoint-derived potential-temperature perturbations (about 2 K). The magnitudes of the adjoint and wave perturbations are comparable to those of initial-condition uncertainties from present-day data assimilation systems (Doyle et al. 2014). To investigate the sensitivity of the error growth to the initial magnitude, we also run identical-twin experiments with the perturbation magnitudes reduced by factors of 10 and 100.

3. Changes to the cyclone

We begin our analysis by focusing on the changes to the cyclone's intensity and to its accompanying precipitation through 48-h lead times. Figure 4a depicts the differences in minimum surface pressure between the perturbed and control runs, and Fig. 4b shows the neighborhood-based fractions skill score (FSS; Roberts and Lean 2008) for precipitation, computed as in Weyn and Durran (2019) with a threshold of $1\ \mathrm{mm\ h^{-1}}$ and a neighborhood of radius 16 km ($4\Delta x$). A perfect FSS of 1 implies that, in the neighborhood around every point, the forecast and the verification have the same fraction of cells with precipitation above the threshold. A completely missed forecast has an FSS of 0, and a score of 0.5 is considered the lower limit of skill in the verification of real-world forecasts (Roberts and Lean 2008).

Only the full-magnitude adjoint perturbations produce a significant change to the surface cyclone and its accompanying precipitation by 48 h. This is illustrated quantitatively by Fig. 4a, which shows that the adjoint perturbations cause the low pressure center to be more than 8 hPa deeper than in the control simulation, and by Fig. 4b, which shows that only the full-magnitude adjoint perturbations produce an FSS below 0.5. These impacts are also illustrated qualitatively by the plots of surface pressure and composite reflectivity in Fig. 5. The adjoint perturbations not only deepen the cyclone significantly, but also move the low pressure center several hundred kilometers to the northwest, move the cold front and its associated convection to the northeast, and intensify the precipitation such that the maximum accumulated precipitation is 2.5 times larger than that of the control simulation.

In contrast, the full-magnitude wave perturbations strongly affect the convection early in the forecast period, but the subsequent upscale error growth does not significantly affect the intensity of the surface cyclone, and it does not change the large-scale distribution of precipitation. Instead, the random displacement of convective cells by the small-scale-wave perturbations becomes negligible by 48 h because the mostly unchanged synoptic-scale flow modulates the development of convection. This is demonstrated by the FSS for the full-magnitude wave case (Fig. 4b), which drops below 0.7 in the first 12 h due to the redistribution of the convection, but then increases to 0.9 over the remaining 36 h as the precipitation becomes more strongly influenced by the synoptic-scale baroclinic development. At 48 h, the differences in reflectivity are primarily localized to individual convective cells, the minimum surface pressure is only 0.85 hPa deeper than the control, and the low is generally in the same location (Fig. 5).

Notably, the 1/10-magnitude adjoint perturbations produce greater changes to the cyclone's intensity (Fig. 4a) by 48 h than the full-magnitude wave perturbations. Nevertheless, the changes produced by the 1/10-magnitude perturbations of

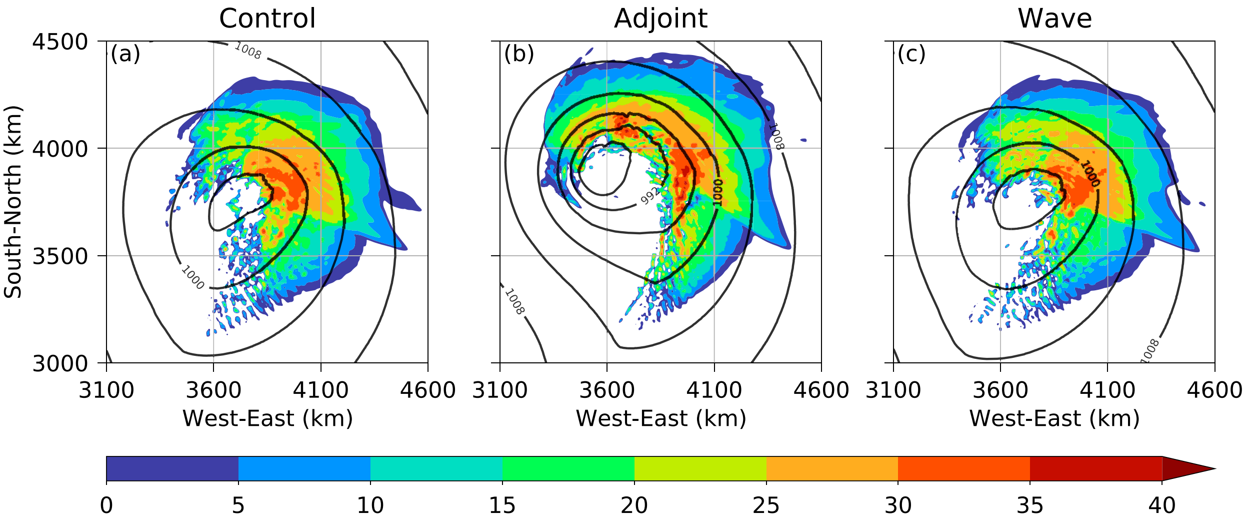

FIG. 5. Modeled composite reflectivity (color fill every 5 dBZ) and surface pressure (black contours every 4 hPa) for (a) the control simulation and for the simulations with the full-magnitude (b) adjoint and (c) wave perturbations at 48-h lead times.

both types do not correspond to a significant displacement of the low pressure center nor its accompanying precipitation at 48 h, as shown by Figs. 4 and 6. For both 1/10-magnitude experiments, the differences in precipitation are primarily localized to individual convective cells, and the 48-h FSS for both cases is about 0.9. For the 1/100-magnitude experiments, the adjoint perturbations produce a slightly lower FSS than the wave perturbations at 48 h (Fig. 4b), but the changes to the surface pressure and composite reflectivity produced by both perturbation types are negligible (not shown).

4. Error-growth dynamics

a. DTE growth

The goal of this section is to consider the error-growth dynamics involved in the changes to the midlatitude cyclone discussed in the previous section. We begin by examining the growth of the domain-integrated DTE, shown in Fig. 7 on both log-linear and linear plots. The errors produced by the full-magnitude adjoint perturbations clearly grow much more rapidly than those produced by the full-magnitude wave perturbations. Even when the magnitude of the adjoint perturbations is reduced by a factor of 10, by 48 h the errors outgrow those produced by the full-magnitude wave perturbations. Unsurprisingly, the 1/10-magnitude adjoint perturbations also generate much larger DTE than the 1/10-magnitude wave perturbations.

When the initial magnitudes are reduced by a factor of 100, the DTE grows almost identically by over four orders of magnitude for both types of perturbations through 33 h. Notably, there is nearly identical monotonic DTE growth over the first 12 h (Fig. 7a), showing that the initial growth of the wave

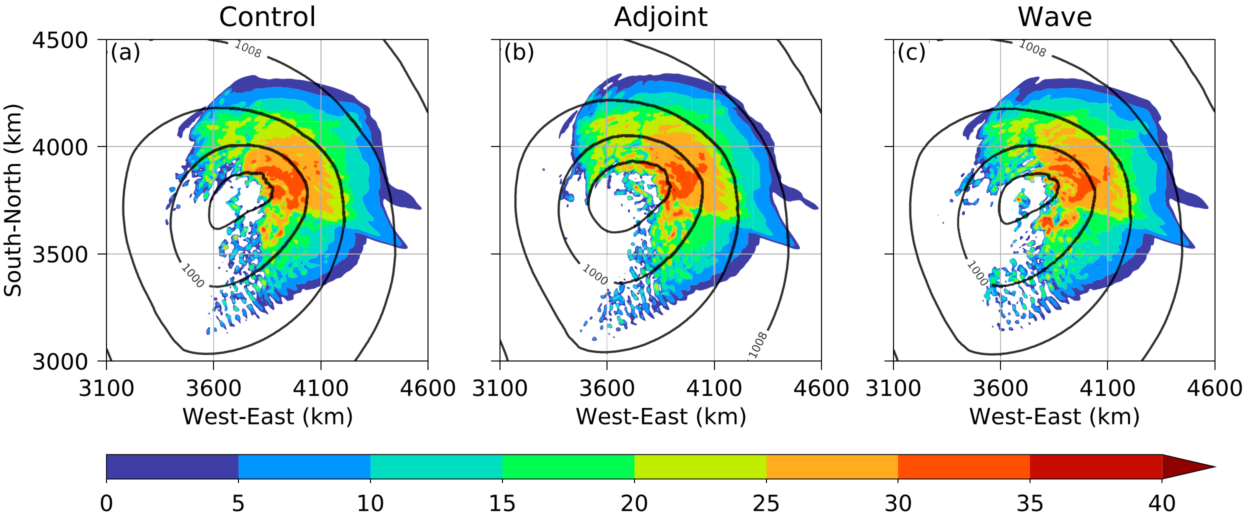

FIG. 6. As in Fig. 5, but for the simulations with the 1/10-magnitude perturbations.

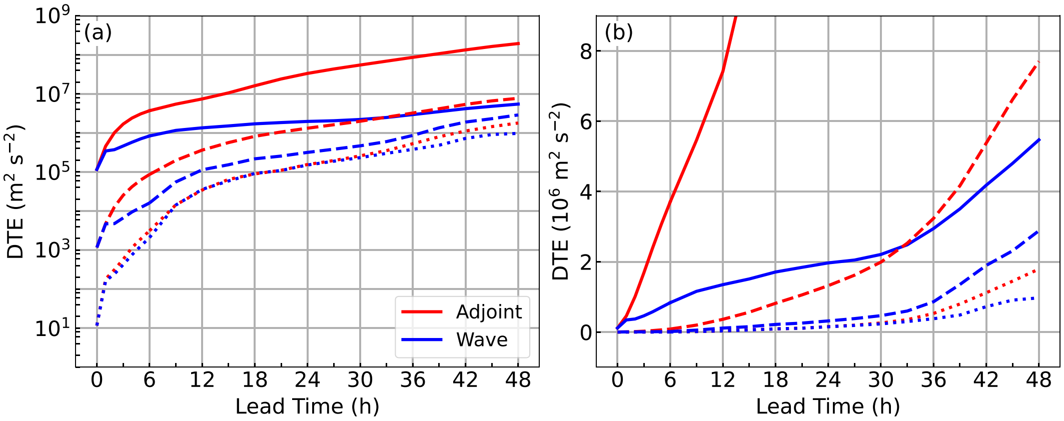

FIG. 7. (a) Time series of the domain-integrated difference total energy (DTE) through 48-h lead times for the experiments with the adjoint (red) and wave (blue) perturbations. The solid, dashed, and dotted lines correspond to the full-, 1/10-, and 1/100-magnitude experiments, respectively. (b) As in (a), but with a linear ordinate axis instead of logarithmic.

perturbations is not inhibited relative to the adjoint perturbations by processes like dissipation or dispersion (both physical and numerical) and suggesting that both types of perturbations are adequately resolved by the numerical model.

b. *Upscale error growth*

Deep cumulus convection is a rapidly growing instability, and perturbations to the locations of convective cells can quickly generate large-magnitude forecast errors locally. It is well established that the low-frequency response to a fixed heat source develops a large-scale cyclonic rotation due to the action of the Coriolis force, both in an environment with no mean flow (Bierdel et al. 2017, 2018) and with vertical wind shear (Pandya et al. 2000). Perturbations to the cumulative heating in mesoscale convective systems have therefore been identified as an important avenue for the upscale transfer of errors from convective to synoptic scales (Zhang et al. 2007; Selz and Craig 2015; Baumgart et al. 2019). Midlatitude cyclones grow through a different type of atmospheric flow instability, and errors associated with misrepresentations of this baroclinically unstable growth can develop directly on much larger scales than those initially generated by errors in forecasts of convection. Here we compare the characteristics of the upscale error growth produced by the adjoint and wave perturbations.

Figure 8 shows the 500-hPa meridional-wind differences (δv) at 12-h lead times. As shown in Fig. 7a, the initial periods of very rapid DTE growth have finished by 12 h, and the ensuing errors in each simulation continue to amplify at a more nearly uniform quasi-exponential rate. The largest-absolute-magnitude δv in each experiment appear to be associated with moist convection, but unsurprisingly, the differences produced by the full-magnitude adjoint perturbations are larger than in the other cases, both in magnitude and scale. The maximum magnitude of the δv generated by the 1/10-magnitude adjoint and full-magnitude wave perturbations are similar, although the differences produced by the full-magnitude wave perturbations extend over a broader region, leading to the larger value of 12-h DTE in Fig. 7. Also of note is that most of the locations with extrema in δv in the 1/10-magnitude adjoint coincide with the locations of extrema of similar sign in the full-magnitude adjoint, although there are additional regions of with strong δv in the full-magnitude case where no strong response appears in the 1/10-magnitude case. The 1/10-magnitude wave perturbations produce weaker and more localized δv than those of the corresponding adjoint case. Finally, the δv in both 1/100-magnitude cases are similar in both strength and limited spatial extent, consistent with their similar 12-h DTE values (Figs. 8c,f).

Despite having less DTE at 12 h, the subsequent upscale error growth in the 1/10-adjoint case is substantially faster than that of the full-magnitude wave case. The faster growth of the adjoint perturbations is particularly evident at lower levels, as demonstrated by the vertical profiles of DTE at 48-h lead times (Fig. 9). Although there is a substantial contrast in magnitude between the errors in the full-magnitude adjoint and those of the other experiments (Fig. 9a), the vertical structure of DTE is qualitatively similar in each of the experiments, with relative maxima near the surface and in the upper troposphere. Nevertheless, the *absolute* maxima in DTE are at low levels in the full- and 1/10-magnitude adjoint cases, whereas they are in the upper troposphere (between 350 and 400 hPa) in the corresponding experiments with wave perturbations. Notably, the DTE produced by the 1/10-magnitude adjoint perturbations is about equal to that of the full-magnitude wave perturbations in the upper troposphere, but is much greater in the lower troposphere. This suggests that both perturbations produce differences in moist convection that similarly project onto the upper troposphere (Bierdel et al. 2017; Baumgart et al. 2019), but that randomly perturbing the convection does not alter the synoptic-scale baroclinically unstable flow enough to produce a very strong response at low levels.

c. *Importance of nonlinearity*

The Lorenz (1969) model, which introduced the idea of upscale error growth through scale interactions, linearizes the

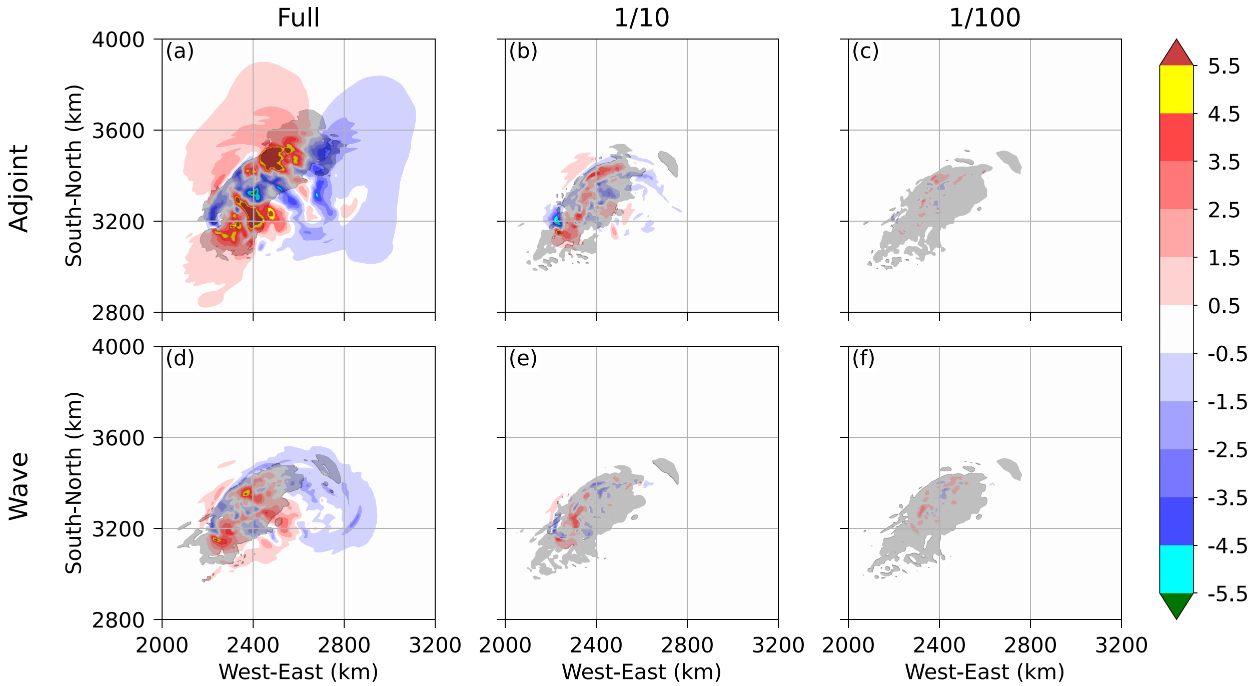

FIG. 8. The 500-hPa meridional-wind differences between the perturbed and control simulations (color fill every 1 m s^{-1}) at 12-h lead times for the experiments with the (a),(d) full-, (b),(e) 1/10-, and (c),(f) 1/100-magnitude (a)–(c) adjoint and (d)–(f) wave perturbations. The gray shading indicates where the modeled composite reflectivity exceeds 5 d*BZ*.

equations for the mean error growth in an ensemble of solutions to the nonlinear two-dimensional vorticity equation for incompressible flow. Because of this linearization, all scale interactions involve the product of nominally small-magnitude ensemble-mean errors (perturbation streamfunction ϵ' in Lorenz's notation) at one scale with the fixed structure of the unperturbed flow (streamfunction ψ in Lorenz's notation) at a second scale. Lorenz solves a system of linear evolution equations for $\epsilon'^2(t)$ and includes nonlinearity by halting the growth with time at each wavenumber k when the error KE at that wavenumber saturates: essentially when $\epsilon_k'^2(t)$ equals ψ_k^2 (although Lorenz actually employs equations in which the

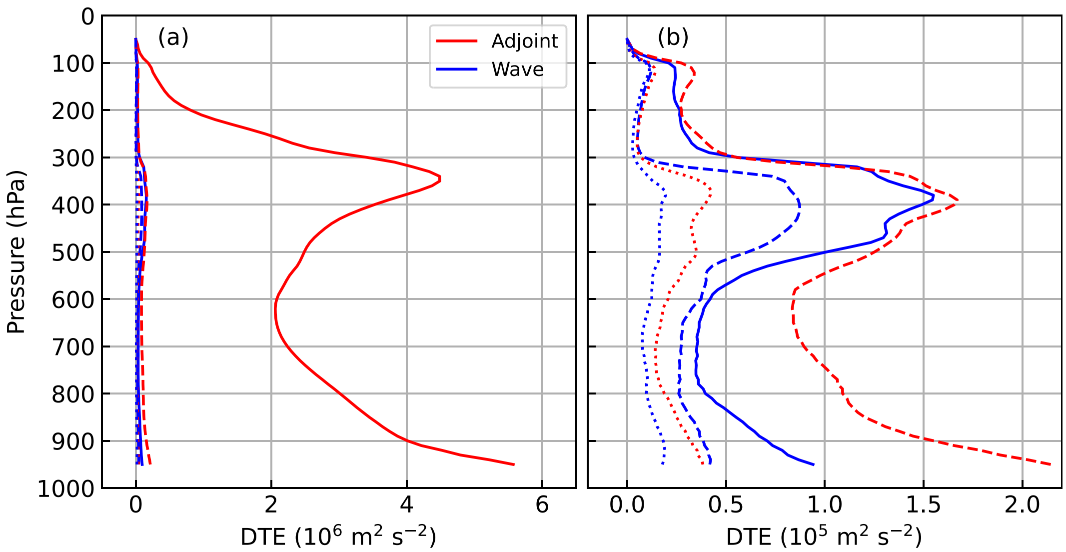

FIG. 9. (a) Vertical profiles of horizontally integrated DTE at 48-h lead times for the experiments with the adjoint (red) and wave (blue) perturbations. The solid, dashed, and dotted lines correspond to the full-, 1/10-, and 1/100-magnitude experiments, respectively. (b) As in (a), but with the full-magnitude adjoint excluded.

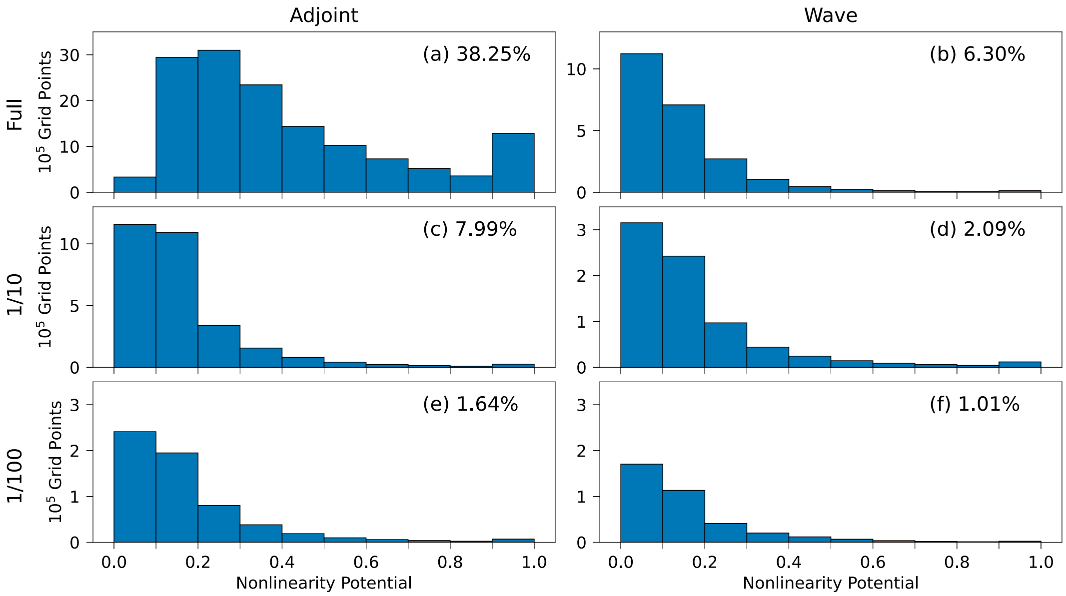

FIG. 10. Histograms for the nonlinearity potential, as defined by (10), at 48-h lead times. Percentages refer to the number of grid points at which the wind and temperature differences between the control and perturbed simulations exceed 0.1 (m s^{-1} and K) out of the possible points at which the wind and temperature differences between the control simulation and the background state exceed 1.0 (m s^{-1} and K). (a),(c),(e) The full-, 1/10-, and 1/100-magnitude adjoint experiments, respectively. (b),(d),(f) The full-, 1/10-, and 1/100-magnitude wave experiments, respectively. Note the variations in scale along the ordinate axis.

variables and the wavenumber intervals have been transformed to facilitate their solution).

The assumption of linear error growth all the way to saturation is clearly questionable in the case of forecast busts, which by definition, require significant differences between the control and perturbed simulations (i.e., the magnitude of the differences between the control and perturbed simulations must approach or exceed that of the total fields in the control simulation). In other words, there must be a nontrivial set of points at which the linearization hypothesis, that the differences are small compared to the total fields, breaks down. To estimate the possible importance of nonlinear dynamics in our experiments, we compute the nonlinearity potential at each grid point, defined as

$$R_{\mathrm{np}} = \frac{1}{3}\left(\frac{|\delta u|}{|U|} + \frac{|\delta v|}{|V|} + \frac{|\delta T|}{|T|}\right), \qquad (10)$$

where δu, δv, and δT are the differences between the perturbed and control simulations for zonal and meridional wind and temperature, and U, V, and T are the differences between the control simulation and the zonally uniform background state for zonal and meridional wind and temperature.

The term R_{np} represents the potential for nonlinearity in the sense that it must be small for the a priori validity of the hypothesis that the dynamics of the perturbation flow about the control simulation are linear. It is not a sufficient condition for the dynamics to be nonlinear, nor does its magnitude necessarily indicate the importance of nonlinear processes in the flow evolution. Nevertheless, there are only a few known special cases (e.g., Long 1953) in which finite-amplitude solutions to the full nonlinear equations of fluid motion are essentially identical to linear solutions.

Figure 10 shows histograms of R_{np} at 48-h lead times. To focus on the portion of the domain with cyclone and anticyclone development, and to prevent division by zero, we neglect all points at which any of the denominators in (10) are less than 1; let this set of points be denoted P. Note that P comprises the same set of points in all of our experiments. Points in P with very small errors (numerators < 0.1) would dominate the histograms and are not plotted; instead, the prevalence of points with nontrivial R_{np} is indicated for each case by the percentage of the points in P for which the numerators are greater than 0.1.

Unsurprisingly, the full-magnitude adjoint experiment exhibits the strongest nonlinearity potential, with 38% of the points in P having error magnitudes large enough to be plotted in the histogram and a large fraction of those points having $R_{\mathrm{np}} > 0.2$ (Fig. 10a). A significant fraction of the points have $R_{\mathrm{np}} > 0.9$, implying that the changes to the cyclone produced by the full-magnitude adjoint perturbations have similar magnitudes to the changes made by the control cyclone to the zonally uniform background state. Both the 1/10-magnitude adjoint and the full-magnitude wave cases develop much lower values of R_{np}. The fraction of points in P with large-enough errors to appear on the histogram is substantially reduced compared to the full-magnitude adjoint case, and most of the weight in each histogram is at R_{np} values less than 0.2 (Figs. 10b,c). Nevertheless, the 1/10-magnitude adjoint case does show somewhat more nonlinearity potential (higher bin

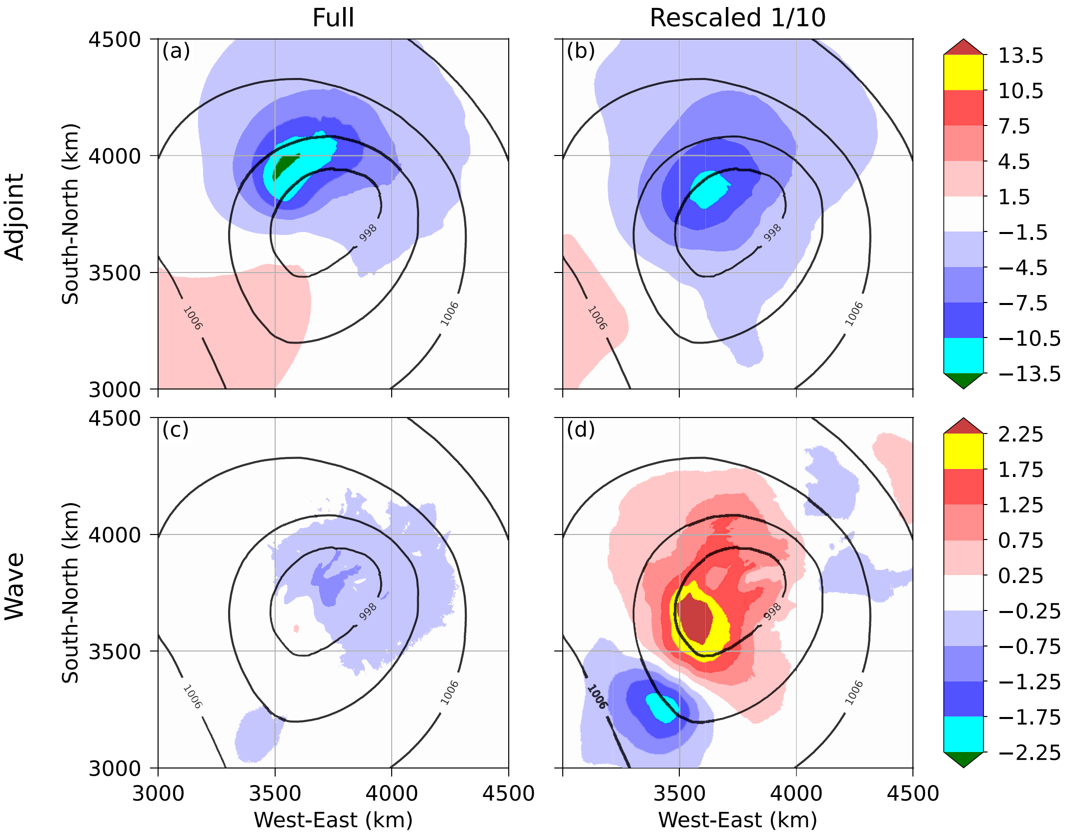

FIG. 11. Differences in surface pressure between the perturbed and control simulations (color fill; hPa) at 48-h lead times for the experiments with the (a),(c) full-magnitude perturbations and (b),(d) 1/10-magnitude perturbations with the differences rescaled following (12). (a),(b) Adjoint-perturbed simulations and (c),(d) wave-perturbed cases. Black contours depict the control simulation's 48-h surface pressure field every 4 hPa.

counts at each R_{np}) than the full-magnitude wave case. In the three other experiments (Figs. 10d–f), the magnitudes of the perturbations about the control simulation remain sufficiently small that nonlinear interactions involving them are likely minimal. Even though the 1/100-magnitude perturbations of both types produce rapid DTE growth by more than four orders of magnitude, at 48 h only 1%–2% of the points in P have large enough errors to appear on the histogram, and most of the points have $R_{\mathrm{np}} < 0.2$.

One way to empirically assess the influence of nonlinear error growth is to run simulations with initial-condition perturbations that are identical in structure but differ in magnitude, and then compare the errors in the evolved solutions after normalizing them by the ratio of their initial magnitudes. If we do this for our full-, 1/10-, and 1/100-magnitude simulations we find that very small-scale convective perturbations in the 1/100 cases dominate the solution. To a lesser extent, this is also a problem in the 1/10 wave case. Therefore, we follow the strategy of Lorenz (1969) and truncate the contributions from scaled-up differences to the magnitudes where their spectral power matches that of the background control simulation.

For example, to compare the full-magnitude surface pressure perturbations with those from the corresponding 1/10-magnitude simulations, we compute the Fourier transform of the perturbations in the 1/10-magnitude pressure field (yielding the kth-wavenumber Fourier component $\widehat{\delta p}_k$). We similarly transform the pressure differences between the control simulation and the zonally uniform background state to yield $\hat{P}_k$. Letting an asterisk denote the complex conjugate, we compute the scaled-up differences in the pressure field $\widehat{\delta\tilde{p}}_k$ as follows. Let

$$c_k = \left(\frac{\widehat{10\delta p}_k\,\widehat{10\delta p}_k^{\,*}}{\hat{P}_k\,\hat{P}_k^{*}}\right)^{1/2}, \qquad (11)$$

then

$$\widehat{\delta\tilde{p}}_k = \begin{cases} \widehat{10\delta p}_k/c_k, & \text{if } c_k > 1, \\ \widehat{10\delta p}_k, & \text{otherwise.} \end{cases} \qquad (12)$$

We then transform this scaled-up perturbation pressure field back to physical space. Compared to the Lorenz (1969) model, this procedure overestimates the influence of small-scale differences that saturate, because Lorenz holds the Fourier components for those scales constant as soon as they saturate, whereas here we only adjust them back to saturation at the end of our simulations.

Figure 11 compares the full-magnitude surface pressure perturbations with those from the corresponding 1/10-magnitude simulations, rescaled as described above. The pressure differences in

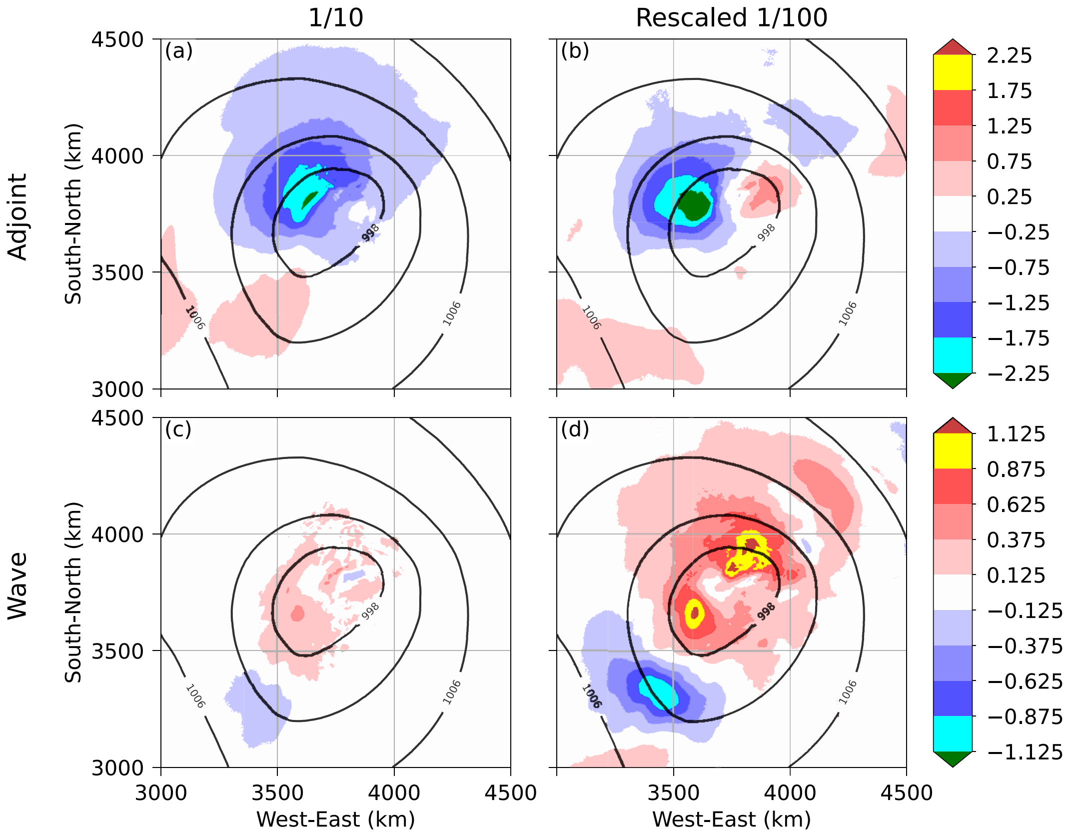

FIG. 12. As in Fig. 11, but for the (a),(c) 1/10-magnitude and (b),(d) rescaled 1/100-magnitude experiments.

the full-magnitude and scaled-up 1/10-magnitude simulations are roughly similar except that the minimum in the full-magnitude case is shifted roughly 200 km to the northwest and is slightly stronger than that in the scaled-up field (Figs. 11a,b). The 200-km shift to the NW of a strong developing cyclone is a significant perturbation to the forecast produced by nonlinear dynamics. The differences between the full-magnitude wave perturbations and the scaled-up 1/10-magnitude case are even more pronounced than those in the adjoint cases, though their absolute magnitudes are much smaller (note the difference in the color scale). The full-magnitude wave perturbation generates modest decreases of about 1 hPa slightly northwest of the low center, while the scaled-up perturbation generates 2 hPa surface pressure rises just southwest of the low center and is part of a couplet of pressure changes that extends farther to the southwest (Figs. 11c,d). There is no reason to expect that small-scale-wave perturbations should necessarily either deepen or fill the cyclone, but the contrast between the full-magnitude and scaled-up differences in surface pressure is nevertheless notable, and is again produced by nonlinear processes.

Repeating the previous analysis, but scaling up the 1/100-magnitude perturbations to 1/10 magnitude, yields the results shown in Fig. 12. The 1/100-magnitude adjoint differences scale up to give a field generally similar to the differences in the 1/10-magnitude adjoint case (Figs. 12a,b). Moreover, in contrast to the result obtained from rescaling the larger-magnitude adjoint perturbations, there is no shift in the location of greatest pressure falls. Scaling up the results from the 1/100-magnitude wave case yields some significant differences compared to the 1/10-magnitude wave case, but unlike the situation in Fig. 11, there is still an obvious gross similarity in the distribution of pressure rises and falls (Figs. 12c,d).

Another way to examine the contributions from nonlinear dynamics is to compare solutions from the tangent-linear model used to compute the adjoint with those from the nonlinear model after starting both from the same adjoint-derived initial conditions. We provide this comparison in Fig. 13. As is typical, the tangent-linear model overamplifies the solution, but interestingly, it continues to place the region of maximum deepening roughly 200 km to the southeast of its actual location in the nonlinear simulation, the same location obtained when scaling up the 1/10- and 1/100-magnitude adjoint perturbations using (11) and (12). As is well known and illustrated in our comparison of the tangent-linear and nonlinear solutions, nonlinear processes do regulate the otherwise unchecked growth of linear modes, but this should not be interpreted as meaning they do not play a key role in forecast busts. Instead, the results in Figs. 11–13 suggest that nonlinear dynamics plays a crucial role in the forecast bust by displacing the low-center relative to the locations computed by linear solutions.

The preceding analysis suggests that nonlinear error interactions start to become important in the adjoint cases when

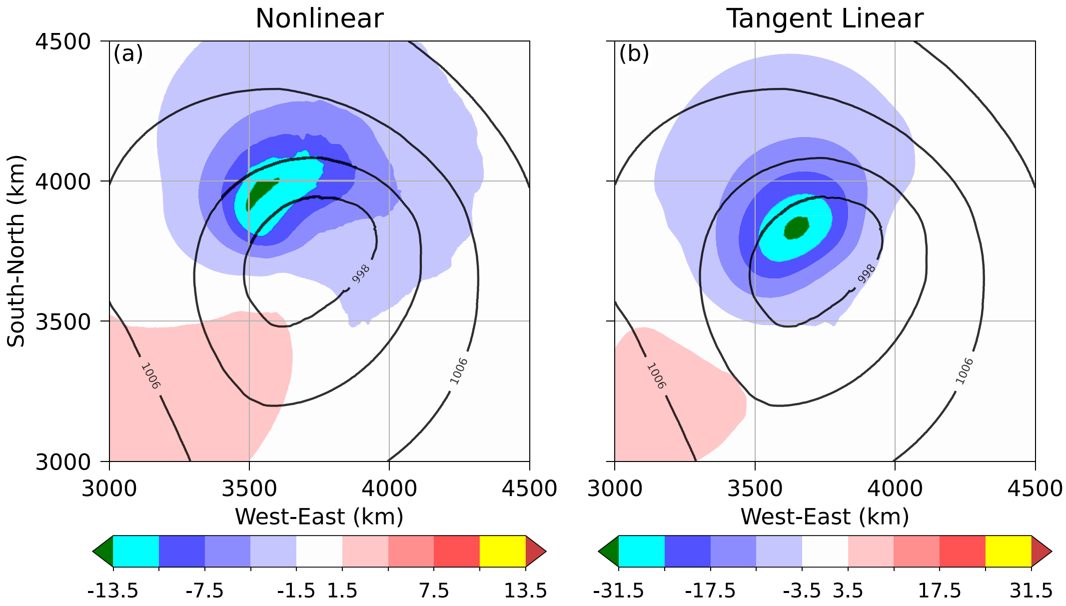

FIG. 13. Surface pressure differences (color fill; hPa) at 48-h lead times for the full-magnitude adjoint perturbations evolved in the (a) nonlinear and (b) tangent-linear models. Black contours depict the nonlinear control simulation's 48-h surface pressure field every 4 hPa.

many points exhibit values of $R_{\mathrm{np}} > 0.2$ (Fig. 10a). This intuitively reasonable result does not hold in the case of the wave perturbations, which even at full magnitude are not sufficient to produce many points with values of $R_{\mathrm{np}} > 0.2$ (Fig. 10b), nor a forecast bust (Fig. 5c). Nevertheless, despite the reduced magnitude of their induced errors, nonlinear dynamics appear to play a major role in the difference between the full- and 1/10-magnitude wave cases, perhaps because error growth in these cases is more tightly linked to deep convection, which is a highly nonlinear process.

d. *Approach to geostrophic balance on synoptic scales*

A common way to assess the effect of upscale error growth on the large-scale flow is to consider the evolution of the errors toward geostrophic balance on synoptic scales (Zhang et al. 2007; Selz and Craig 2015). To address this, we filter the wind and height fields, removing wavelengths smaller than 1000 km, and plot the geostrophic and ageostrophic components of the large-scale wind differences. For this part of the analysis, we focus on the wind differences at 350 hPa because this is roughly the level at which the errors produced by upscale growth from convection are greatest (Fig. 9b).

Figure 14 shows that at 48-h lead times, the balanced synoptic-scale wind differences are characterized by an anticyclonic circulation with wind speeds of about 5 and 1 m s^{-1} in the full- and 1/10-magnitude adjoint experiments, respectively. The balanced vortices are roughly centered above the regions of heavy precipitation shown in Figs. 5b and 6b, as would be consistent with the balanced upper-level response to a steady mesoscale-convective heat source in a frame of reference moving with the mean flow (Bierdel et al. 2017). A hint of the same balanced anticyclonic circulation is present in the full-magnitude wave case, but despite having similar convectively generated extrema and more widespread δv than in the 1/10-magnitude adjoint case at 12 h (Figs. 8b,d), the circulation in the full-magnitude wave case is clearly weaker. The large-scale balanced circulations in the other three cases are more random.

Taking the characteristic time scale for the appearance of balanced flow in response to a fixed heat source as $t_{\mathrm{GA}} = 3.8f^{-1} \approx 10$ h (Bierdel et al. 2017), and assuming that significant differences in convective heating are established by 18 h in both pairs of full- and 1/10-magnitude cases (Fig. 4b), the 48-h differences in Figs. 14a–d correspond to times of at least $3t_{\mathrm{GA}}$. Yet the balance, indicated by the relative lengths of the red ageostrophic and black geostrophic wind vectors, is poor in both experiments with wave perturbations. Geostrophic balance is most nearly satisfied by the full-magnitude adjoint and is essentially nonexistent in both 1/100-magnitude cases.

If the errors have more time to grow, do they become closer to geostrophic balance? To address this possibility, we extend the simulations out to 96-h lead times ($7t_{\mathrm{GA}}$ after significant differences in convective heating). Figure 15 shows that at this lead time the balanced synoptic-scale wind differences in the full-magnitude adjoint experiment are still characterized by an anticyclonic circulation downstream of the upper-level ridge; meanwhile, a cyclonic circulation has developed downstream of the upper-level trough. There is a similar, but weaker response in the 1/10-magnitude adjoint case, and the anticyclonic differences are much weaker than the cyclonic differences. There also appears to be a hint of these perturbation patterns in the full-magnitude wave case, but the ageostrophic component of the differences is nearly equal to the geostrophic component, suggesting that the synoptic-scale differences are still substantially unbalanced even after 48 h of additional growth. While the synoptic-scale wind differences

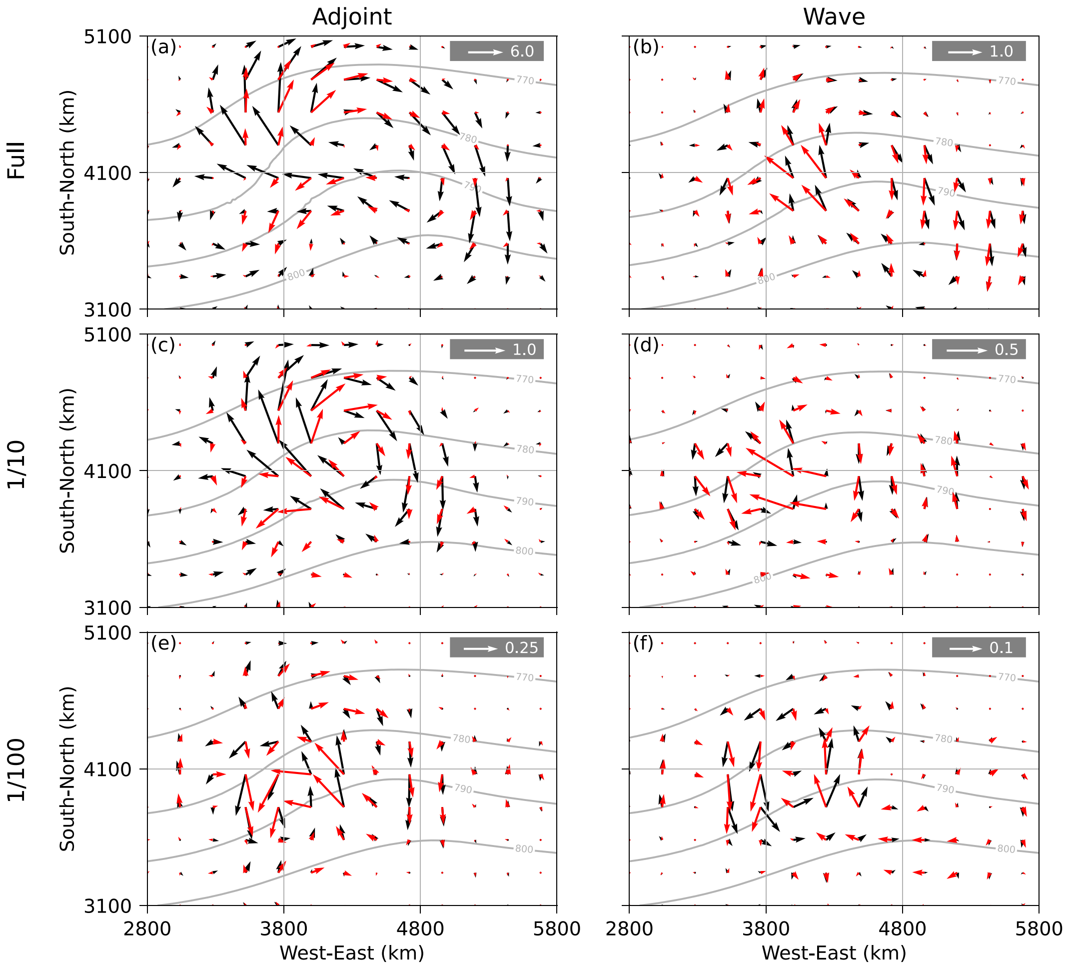

FIG. 14. The 350-hPa horizontal-wind differences between the perturbed and control simulations at 48-h lead times, with wavelengths smaller than 1000 km filtered out. Black arrows correspond to the geostrophically balanced component of the total difference wind, while red arrows correspond to the ageostrophic component. Reference magnitudes in m s^{-1} are provided in the gray boxes. Gray contours depict the 350-hPa geopotential height for the perturbed simulation every 10 dam. (a),(c),(e) The full-, 1/10-, and 1/100-magnitude adjoint experiments, respectively. (b),(d),(f) The full-, 1/10-, and 1/100-magnitude wave experiments, respectively.

in the 1/10-magnitude wave and in both 1/100-magnitude cases are stronger than at 48 h, they remain quite random and geostrophically unbalanced.

To provide a more quantitative, domain-integrated assessment of the approach to geostrophic balance on synoptic scales, we compute the ratio

$$R_{\mathrm{ag}} = \frac{\|\Delta \mathbf{V}_{\mathrm{ag}}\|}{\|\Delta \mathbf{V}_{g}\|}, \tag{13}$$

where $\|\Delta \mathbf{V}_{\mathrm{ag}}\|$ and $\|\Delta \mathbf{V}_{g}\|$ are the domain-averaged magnitudes of the ageostrophic and geostrophic components, respectively, of the filtered large-scale wind differences. Because neither the total synoptic-scale wind fields, nor the errors, are expected to be in exact geostrophic balance, we also evaluate a measure of the less-restrictive nonlinear balance derived by Charney (1955). To this end, we compute the ratio of the divergence over the vorticity, defined by Selz and Craig (2015) as

$$R_{\mathrm{dv}} = \sqrt{\frac{\|\Delta D\|}{\|\Delta \zeta\|}}, \tag{14}$$

where $|\|\Delta D\||$ and $\|\Delta \zeta\|$ are the domain-averaged squared differences in horizontal divergence and relative vorticity, respectively, of the filtered large-scale wind differences.

Figure 16 depicts the evolution of these two ratios through 96 h of forecast lead time for each of our experiments, and for the total fields in the control simulation. For the total fields in the control simulation, both R_{ag} and R_{dv} are below 0.2 throughout the 96-h period, indicating that the (filtered) synoptic-scale component of the full unperturbed flow is close to balance.

Focusing on the difference fields, both ratios initially exceed unity in all experiments, but evolve toward increasing balance over the 96-h period, with the full-magnitude adjoint case being the most nearly balanced and both 1/100-magnitude cases the least balanced. The relative degrees of balance between

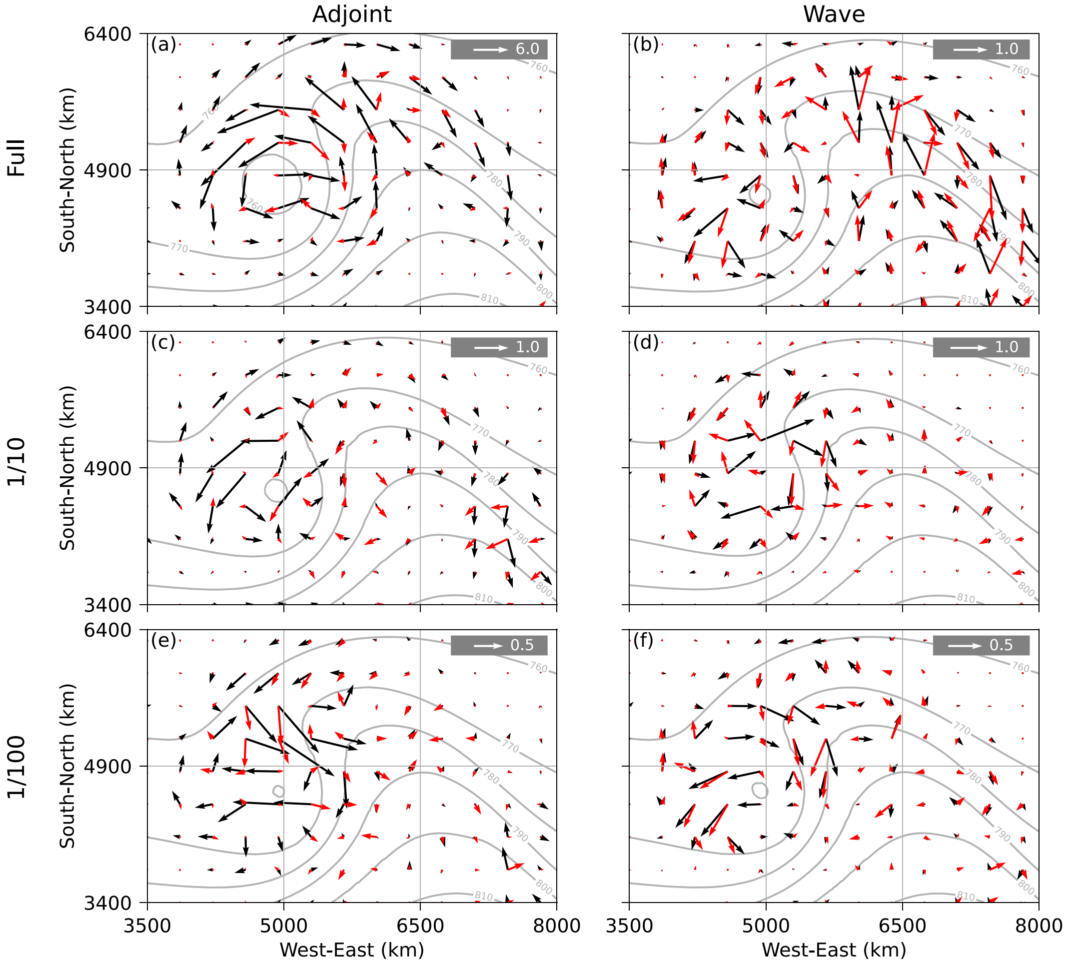

FIG. 15. As in Fig. 14, but at 96-h lead times.

the experiments depicted by these ratios are qualitatively consistent with the 350-hPa wind differences shown in Figs. 14 and 15.

There are, however, significant quantitative differences between the R_{ag} and R_{dv} ratios, especially at early lead times. The adjustment toward geostrophic balance is slow, and the 1/10- and 1/100-magnitude wave experiments actually experience an increase in R_{ag} over the first 24 h. Despite a steady decrease in R_{ag} for all experiments over the subsequent 72 h, only the full-magnitude adjoint case has a value below 0.5 by 96 h. In contrast, each experiment experiences a much more rapid decrease in R_{dv} over the first 24 h, especially for the adjoint perturbations of all magnitudes and the full-magnitude wave perturbations. At 96 h, all experiments have values of R_{dv} at or below 0.5, indicating that the errors are substantially closer to nonlinear balance than they are to geostrophic balance.

5. Sensitivity to the stage of the cyclone's development

The results discussed up until this point correspond to error growth starting from an early stage of the cyclone's development. To test the generalizability of these results to more mature midlatitude cyclones, we also conduct identical-twin experiments with perturbations added at 72 and 96 h into the control simulation. The procedure for computing the adjoint and wave perturbations at these times follows that of the 48-h perturbations described in sections 2b and 2c.

Figure 17 compares the error growth corresponding to the full-magnitude perturbations added at 48, 72, and 96 h into the control simulation. We compute the domain-integrated DTE as in (9), but we divide this value by the DTE corresponding to the differences between the control run and the zonally uniform background state. We use this normalization to account for the fact that the cyclone is larger and more intense at later stages of development. Notably, the adjoint perturbations added at 48 h produce significantly greater normalized DTE (Fig. 17a), with the curves corresponding to the 72- and 96-h adjoint perturbations remaining constant from 36 through 48 h of lead time because, at these later times, the growth rate of the differences is nearly equal to the growth rate of the developing cyclone in the control simulation. Additionally, the 48-h adjoint perturbations produce twice as great of a difference in minimum surface pressure at 48 h of lead time, although the 72-h adjoint perturbations produce a

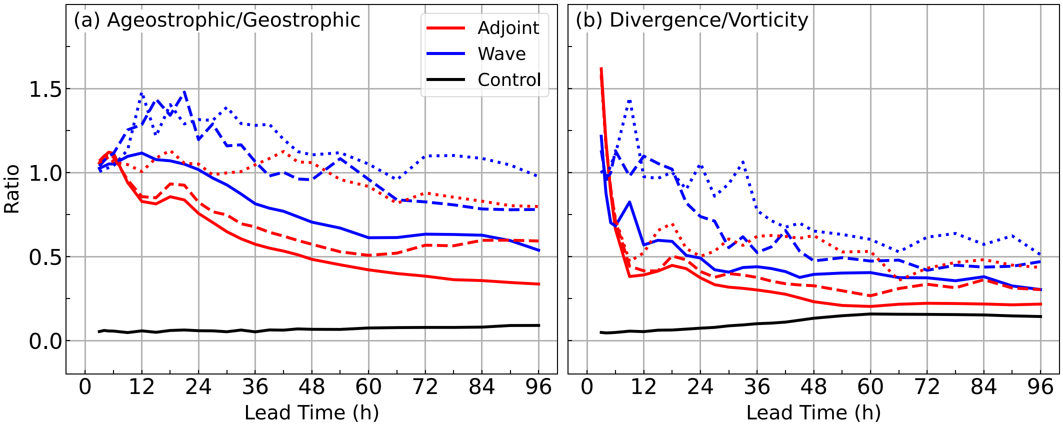

FIG. 16. Time series of large-scale-balance ratios through 96-h lead times for the experiments with adjoint (red) and wave (blue) perturbations. The colored solid, dashed, and dotted lines correspond to the full-, 1/10-, and 1/100-magnitude experiments, respectively. The solid black lines show ratios for the total fields in the control simulation. (a) The ratio of the ageostrophic-wind magnitude over the geostrophic-wind magnitude, as defined by (13). (b) The square root of the ratio of the divergence norm over the vorticity norm, as defined by (14).

stronger response in surface pressure at earlier lead times. At all perturbation times, the full-magnitude wave perturbations produce substantially smaller changes to both the DTE and the cyclone's intensity.

These results are illustrated qualitatively by Figs. 18 and 19, which depict the 48-h lead time forecasts for surface pressure and composite reflectivity when full-magnitude perturbations are added at 72 and 96 h into the control simulation, respectively. For all perturbation times, the changes produced by the wave perturbations are negligible. Although the 72-h adjoint perturbations do move and intensify both the low pressure center and the precipitation, these changes are smaller than those produced by the adjoint perturbations added at 48 h (cf. Fig. 5). At 96 h, the differences are even less significant. These results are consistent with the metrics in Fig. 17, suggesting that early stage cyclones may be particularly sensitive to large-scale perturbations that alter the baroclinic life cycle, whereas the continued development of more mature midlatitude cyclones may be more set in stone. Alternatively, the central pressure response function used for the adjoint runs may not be the most appropriate for mature midlatitude cyclones that have high-impact weather occurring far from the cyclone center; choosing a response function based on precipitation as in Doyle et al. (2019), for example, may lead to more substantial changes to the forecast. This possibility, as well as the potential sensitivity of the error growth to other aspects of the baroclinic life cycle, are worthwhile avenues for future research.

6. Conclusions

In this study we investigate the predictability of a prototypical midlatitude cyclone developing in a moist baroclinically unstable channel. We focus on initial-condition uncertainties that lead to "forecast busts" in which the location and

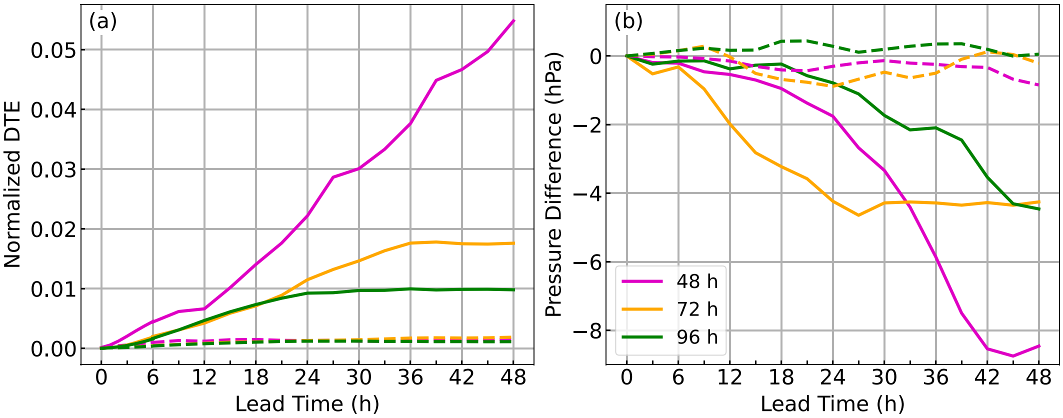

FIG. 17. Time series of (a) normalized DTE (see text) and (b) differences in minimum surface pressure between the control and perturbed simulations through 48-h lead times for the experiments with the full-magnitude perturbations added at 48 (magenta), 72 (orange), and 96 h (green) into the control simulation. The solid and dashed lines correspond to the adjoint and wave perturbations, respectively.

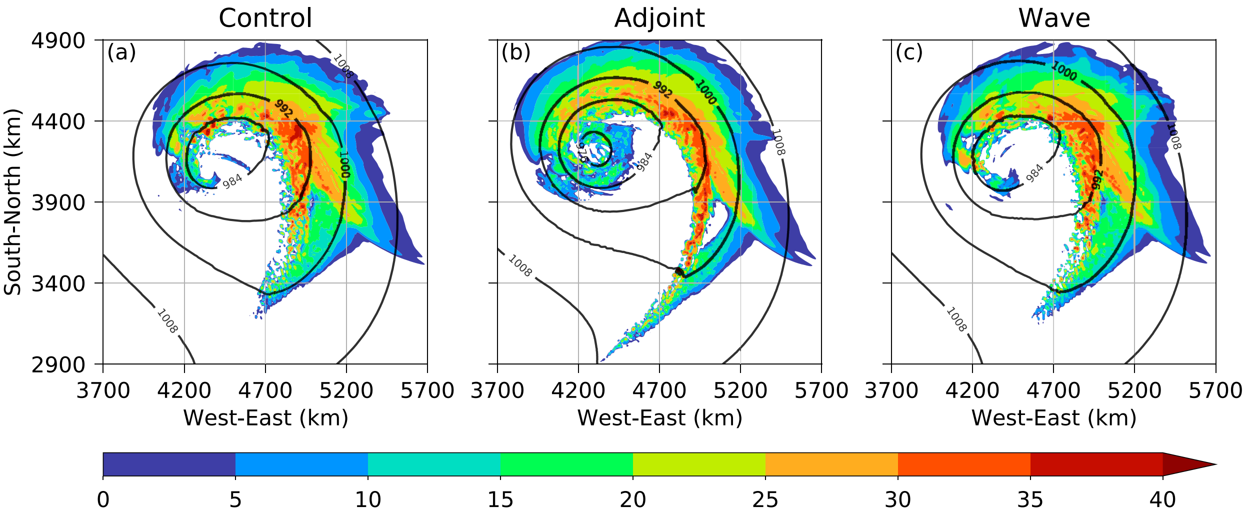

FIG. 18. As in Fig. 5, but for the experiments with perturbations added at 72 h into the control simulation.

intensity of the low and its accompanying precipitation are significantly modified.

Initial-condition perturbations determined from a moist adjoint model, with maximum magnitude of 1 K in potential temperature, trigger much more rapid error growth than equal-energy-norm, small-scale-wave perturbations with maximum magnitude of about 2 K in potential temperature. The full-magnitude adjoint case is the only one among our numerical experiments that produces a genuine forecast bust at a 48-h lead time (Figs. 5a,b). Reducing the magnitude of the adjoint perturbations by a factor of 10 still produces greater 48-h errors than those generated in the full-magnitude wave case, although at earlier times (between 6 and 24 h) the wave perturbations produce somewhat greater errors. In all three of these experiments, the largest-absolute-magnitude differences between the control and perturbed simulations are associated with moist convection, but instead of individual cells randomly interacting to amplify the error, differences in the synoptic-scale flow drive differences in the distribution of convection.

One signature of the extent to which convection is modulated by the developing synoptic-scale cyclone is in the evolution of the fractions skill score (FSS) measuring the difference in the precipitation distribution between the control and perturbed simulations (Fig. 4b). In both the full-magnitude wave and 1/10-magnitude adjoint cases, there is a substantial degradation in the FSS from 6 to 24 h after the perturbations are added. However, despite the continued growth in the intensity and extent of the precipitation in the developing cyclone, by 48 h the FSS has greatly improved, suggesting there is no longer any significant difference in the precipitation fields between the control and perturbed simulations. In contrast, the full-magnitude adjoint perturbations displace the cyclone center by several hundred kilometers and shift the precipitation, creating a forecast bust with FSS values less than 0.5 at all lead times longer than 6 h.

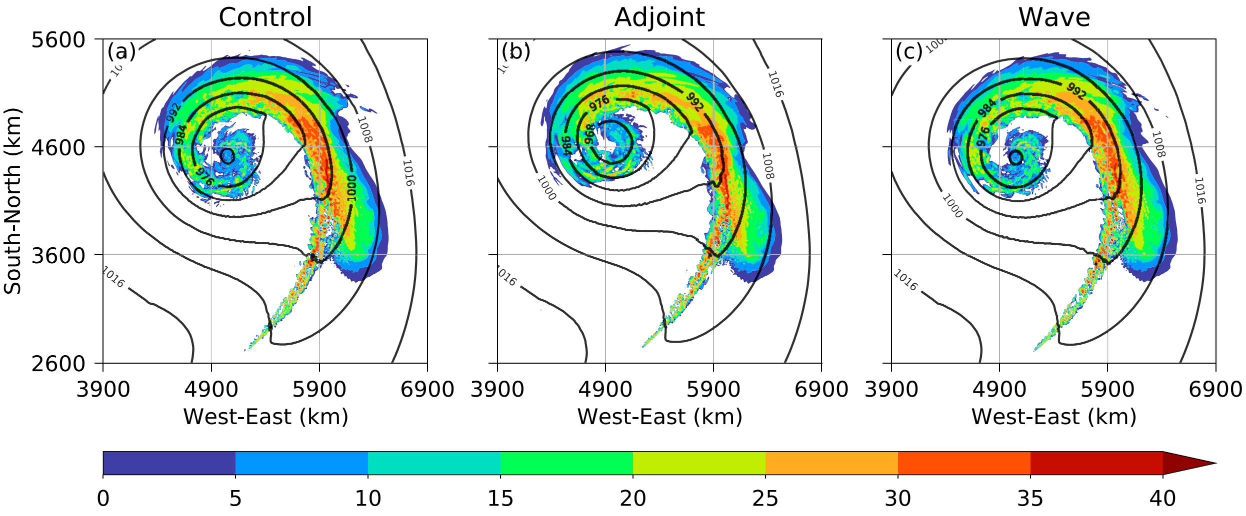

FIG. 19. As in Fig. 5, but for the experiments with perturbations added at 96 h into the control simulation.

The influence of moist convection is also evident in the 48-h synoptic-scale response to the initial-condition perturbations. In the full- and 1/10-magnitude adjoint cases and the full-magnitude wave case, the large-scale wind differences in the upper troposphere are dominated by an anticyclonic circulation at 48 h (Figs. 14a–c), as might be expected due to sustained differences in latent heating (Bierdel et al. 2017). The circulation is strongest and closest to geostrophic balance in the full-magnitude adjoint case, and is weakest and least balanced in the full-magnitude wave case.

Our three other experiments, the 1/10-magnitude wave case and 1/100-magnitude adjoint and wave cases, produce only minor changes to the cyclone and the synoptic-scale flow, even through 96-h lead times. Although they do not come close to causing forecast busts through 2–4-day lead times, the situation with the pair of 1/100-magnitude perturbations is nevertheless noteworthy. In contrast to the four larger-magnitude cases, the DTE values for both 1/100-magnitude cases grow almost identically by four orders of magnitude over the first 33 h (Fig. 7a), yet through 48 h the magnitudes of almost all of the errors remain too small for nonlinear error interactions to be important (Figs. 10e,f and 12). Substantial growth of initially small-magnitude perturbations, independent of their initial horizontal scale, is also a property of the Lorenz (1969) model for error growth in homogeneous isotropic turbulence (Durran and Gingrich 2014). Reminiscent of the empirical behavior in our simulations with the 1/100-magnitude perturbations, the error-growth equations in Lorenz (1969) are linear (except for a nonlinear treatment of error saturation).

Also like our experiments with the 1/100-magnitude perturbations, the relevance of the Lorenz (1969) model to forecast busts involving rapidly developing midlatitude cyclones is tenuous (as opposed to its use in the study of intrinsic predictability limits averaged over many types of weather events). Such cyclones are coherent features (in contrast to homogeneous isotropic turbulence), and significant differences in the position of key cyclone features can be produced by nonlinear error interactions (Figs. 11 and 13). In our simulations, small-magnitude, small-scale perturbations grow upscale too slowly to strongly impact the cyclone through 2–4-day lead times. Although not emphasized by most of their authors, other real and idealized case studies have also found that small-magnitude, small-scale initial-condition errors produce only very minor perturbations to the large-scale flow at forecast lead times ranging from 1.5 to 5 days (Zhang et al. 2007; Selz and Craig 2015; Baumgart et al. 2019).

Of potentially more relevance to midlatitude-cyclone forecast busts is Lorenz's other seminal paper on predictability (Lorenz 1963), which elegantly demonstrated that nonlinear deterministic systems with bounded solutions can exhibit very sensitive dependence on the initial conditions. Contrast this with the upscale error growth in the Lorenz (1969) model, in which the error at a given scale, having any initial magnitude below saturation, inevitably grows and only begins to transfer to the next largest scale when the error in the first scale approaches saturation. A sensitive dependence on synoptic-scale initial conditions, rather than upscale error growth per se, may be the source of most midlatitude-cyclone forecast busts. Over relatively short 2–4-day periods, errors developing directly on synoptic scales may dominate any errors working their way up from very small scales.

We find that our results are broadly similar for midlatitude cyclones at varying stages of baroclinic development (Fig. 17), but examining the sensitivity to different grid spacings or different baroclinically unstable background states is beyond the scope of this study. In particular, faster error growth from the convective scales might be expected in simulations with finer grid spacing (Weyn and Durran 2019) or higher relative humidity and CAPE (Tan et al. 2004). Nevertheless, because the upscale error growth in the unrealistic high-CAPE environment of Zhang et al. (2007) only produced minor large-scale perturbations after 1.5 days, we do not believe that realistic modifications to the thermodynamic fields in our background shear flow would generate sufficiently rapid small-scale error growth to bust a forecast through 2–4-day lead times.

Rapidly developing midlatitude cyclones, while a very important forecast problem, may nevertheless be a special case. Most midlatitude weather is not so directly influenced by a rapidly growing fluid-dynamical instability. For example, the predictability of convective situations with weak synoptic-scale forcing may be particularly sensitive to error growth originating from small scales. Indeed, Flack et al. (2018) found that small-scale perturbations grew upscale more rapidly in convective events over the United Kingdom with weaker synoptic-scale forcing. Similarly, Weyn and Durran (2019) found that convective events over the southeastern United States with weak synoptic-scale forcing were more sensitive to small- than large-scale initial-condition perturbations, whereas the cases with strong forcing were not sensitive to the perturbation scale. The importance of small-scale perturbations likely also applies to the tropics, where synoptic-scale forcing is weaker and interactions among deep convective systems are more dominant. For example, Judt et al. (2016) showed that small-scale perturbations affected the intensity of Hurricane Earl, though consistent with a dominating influence from larger scales, the small-scale perturbations did not impact the cyclone track.

The perturbation structures used in our idealized baroclinic-wave experiments are not intended to directly represent the initial-condition uncertainties in operational forecasting systems. Rather, we intend the adjoint-derived and small-scale-wave perturbations to represent important archetypical perturbations on the synoptic and convective scales, respectively. The extent to which our results apply to practical weather forecasts will depend on how present-day initial-condition errors project onto perturbations of these types. Although they did not focus on forecast busts, the results from Selz et al. (2022) suggest that present-day limits to midlatitude predictability are, on average, dominated by initial-condition errors triggering immediate growth on synoptic scales, as is the case for our experiments with the full-magnitude adjoint perturbations. In addition, since the errors produced by the 1/10-magnitude adjoint perturbations are more significant than those generated by the full-magnitude wave perturbations at 48-h lead times, it does seem likely that analysis errors projecting onto the synoptic and larger mesoscales have the better chance of generating forecast busts. Further research to improve our understanding of the sensitivity of forecast-bust cases to synoptic and mesoscale perturbations is warranted, both in idealized and real-world cases.

Acknowledgments. We are grateful for constructive reviews from Michael Riemer, Chris Snyder, and an anonymous reviewer. We also thank Matthew Fearon for aiding in the transition between the WRF and COAMPS fields. Daniel J. Lloveras and Dale R. Durran acknowledge the support of Grant N00014-20-1-2387 from the Office of Naval Research. James D. Doyle acknowledges the support of the Naval Research Laboratory Base Program through Program Element 0601153N. We acknowledge computational resources from the Navy Department of Defense Supercomputing Resource Center in Stennis, Mississippi.

Data availability statement. The model input and output files used in this study are too large to publicly archive or to transfer. Instead, we provide the information needed to replicate the simulations. The numerical model (WRF version 3.6.1) is publicly available at https://www2.mmm.ucar.edu/wrf/users/download/get_sources.html. The namelist settings for the WRF runs and the Python code for generating the WRF input files are archived with the University of Washington Libraries ResearchWorks repository: http://hdl.handle.net/1773/49482.

REFERENCES

Amerault, C., X. Zou, and J. Doyle, 2008: Tests of an adjoint mesoscale model with explicit moist physics on the cloud scale. *Mon. Wea. Rev.*, **136**, 2120–2132, https://doi.org/10.1175/2007MWR2259.1.

Ancell, B., and G. J. Hakim, 2007: Comparing adjoint- and ensemble-sensitivity analysis with applications to observation targeting. *Mon. Wea. Rev.*, **135**, 4117–4134, https://doi.org/10.1175/2007MWR1904.1.

Baumgart, M., P. Ghinassi, V. Wirth, T. Selz, G. C. Craig, and M. Riemer, 2019: Quantitative view on the processes governing the upscale error growth up to the planetary scale using a stochastic convection scheme. *Mon. Wea. Rev.*, **147**, 1713–1731, https://doi.org/10.1175/MWR-D-18-0292.1.

Bierdel, L., T. Selz, and G. C. Craig, 2017: Theoretical aspects of upscale error growth through the mesoscales: An analytical model. *Quart. J. Roy. Meteor. Soc.*, **143**, 3048–3059, https://doi.org/10.1002/qj.3160.

——, ——, and ——, 2018: Theoretical aspects of upscale error growth on the mesoscales: Idealized numerical simulations. *Quart. J. Roy. Meteor. Soc.*, **144**, 682–694, https://doi.org/10.1002/qj.3236.

Brennan, M. J., G. M. Lackmann, and K. M. Mahoney, 2008: Potential vorticity (PV) thinking in operations: The utility of nonconservation. *Wea. Forecasting*, **23**, 168–182, https://doi.org/10.1175/2007WAF2006044.1.

Charney, J., 1955: The use of the primitive equations of motion in numerical prediction. *Tellus*, **7**, 22–26, https://doi.org/10.3402/tellusa.v7i1.8772.

Crezee, B., H. Joos, and H. Wernli, 2017: The microphysical building blocks of low-level potential vorticity anomalies in an idealized extratropical cyclone. *J. Atmos. Sci.*, **74**, 1403–1416, https://doi.org/10.1175/JAS-D-16-0260.1.

Davis, C. A., and K. A. Emanuel, 1991: Potential vorticity diagnosis of cyclogenesis. *Mon. Wea. Rev.*, **119**, 1929–1953, https://doi.org/10.1175/1520-0493(1991)119<1929:PVDOC>2.0.CO;2.

Doyle, J. D., C. A. Reynolds, C. Amerault, and J. Moskaitis, 2012: Adjoint sensitivity and predictability of tropical cyclogenesis. *J. Atmos. Sci.*, **69**, 3535–3557, https://doi.org/10.1175/JAS-D-12-0110.1.

——, C. Amerault, C. A. Reynolds, and P. A. Reinecke, 2014: Initial condition sensitivity and predictability of a severe extratropical cyclone using a moist adjoint. *Mon. Wea. Rev.*, **142**, 320–342, https://doi.org/10.1175/MWR-D-13-00201.1.

——, C. A. Reynolds, and C. Amerault, 2019: Adjoint sensitivity analysis of high-impact extratropical cyclones. *Mon. Wea. Rev.*, **147**, 4511–4532, https://doi.org/10.1175/MWR-D-19-0055.1.

Durran, D. R., and M. Gingrich, 2014: Atmospheric predictability: Why butterflies are not of practical importance. *J. Atmos. Sci.*, **71**, 2476–2488, https://doi.org/10.1175/JAS-D-14-0007.1.

Flack, D. L. A., S. L. Gray, R. S. Plant, H. W. Lean, and G. C. Craig, 2018: Convective-scale perturbation growth across the spectrum of convective regimes. *Mon. Wea. Rev.*, **146**, 387–405, https://doi.org/10.1175/MWR-D-17-0024.1.

Hakim, G. J., 2000: Climatology of coherent structures on the extratropical tropopause. *Mon. Wea. Rev.*, **128**, 385–406, https://doi.org/10.1175/1520-0493(2000)128<0385:COCSOT>2.0.CO;2.

——, D. Keyser, and L. F. Bosart, 1996: The Ohio Valley wave-merger cyclogenesis event of 25–26 January 1978. Part II: Diagnosis using quasigeostrophic potential vorticity inversion. *Mon. Wea. Rev.*, **124**, 2176–2205, https://doi.org/10.1175/1520-0493(1996)124<2176:TOVWMC>2.0.CO;2.

Hong, S.-Y., Y. Noh, and J. Dudhia, 2006: A new vertical diffusion package with an explicit treatment of entrainment processes. *Mon. Wea. Rev.*, **134**, 2318–2341, https://doi.org/10.1175/MWR3199.1.

Hoskins, B. J., M. E. McIntyre, and A. W. Robertson, 1985: On the use and significance of isentropic potential vorticity maps. *Quart. J. Roy. Meteor. Soc.*, **111**, 877–946, https://doi.org/10.1002/qj.49711147002.

Jiménez, P. A., J. Dudhia, J. F. González-Rouco, J. Navarro, J. P. Montávez, and E. García-Bustamente, 2012: A revised scheme for the WRF surface layer formulation. *Mon. Wea. Rev.*, **140**, 898–918, https://doi.org/10.1175/MWR-D-11-00056.1.

Judt, F., S. S. Chen, and J. Berner, 2016: Predictability of tropical cyclone intensity: Scale-dependent forecast error growth in high-resolution stochastic kinetic-energy backscatter ensembles. *Quart. J. Roy. Meteor. Soc.*, **142**, 43–57, https://doi.org/10.1002/qj.2626.

Klemp, J. B., J. Dudhia, and A. D. Hassiotis, 2008: An upper gravity-wave absorbing layer for NWP applications. *Mon. Wea. Rev.*, **136**, 3987–4004, https://doi.org/10.1175/2008MWR2596.1.

Langland, R. H., R. L. Elsberry, and R. M. Errico, 1995: Evaluation of physical processes in an idealized extratropical cyclone using adjoint sensitivity. *Quart. J. Roy. Meteor. Soc.*, **121**, 1349–1386, https://doi.org/10.1002/qj.49712152608.

——, ——, and ——, 1996: Adjoint sensitivity of an idealized extratropical cyclone with moist physical processes. *Quart. J. Roy. Meteor. Soc.*, **122**, 1891–1920, https://doi.org/10.1002/qj.49712253608.

——, M. A. Shapiro, and R. Gelaro, 2002: Initial condition sensitivity and error growth in forecasts of the 25 January 2000 East Coast snowstorm. *Mon. Wea. Rev.*, **130**, 957–974, https://doi.org/10.1175/1520-0493(2002)130<0957:ICSAEG>2.0.CO;2.

Lloveras, D. J., L. H. Tierney, and D. R. Durran, 2022: Mesoscale predictability in moist midlatitude cyclones is not sensitive to the slope of the background kinetic energy spectrum. *J. Atmos. Sci.*, **79**, 119–139, https://doi.org/10.1175/JAS-D-21-0147.1.

Long, R. R., 1953: Some aspects of the flow of stratified fluids: I. A theoretical investigation. *Tellus*, **5**, 42–58, https://doi.org/10.3402/tellusa.v5i1.8563.

Lorenz, E. N., 1963: Deterministic nonperiodic flow. *J. Atmos. Sci.*, **20**, 130–141, https://doi.org/10.1175/1520-0469(1963)020<0130:DNF>2.0.CO;2.

——, 1969: The predictability of a flow which possesses many scales of motion. *Tellus*, **21A**, 289–307, https://doi.org/10.3402/tellusa.v21i3.10086.

Mansell, E. R., C. L. Ziegler, and E. C. Bruning, 2010: Simulated electrification of a small thunderstorm with two-moment bulk microphysics. *J. Atmos. Sci.*, **67**, 171–194, https://doi.org/10.1175/2009JAS2965.1.

Pandya, R. E., D. R. Durran, and M. L. Weisman, 2000: The influence of convective thermal forcing on the three-dimensional circulation around squall lines. *J. Atmos. Sci.*, **57**, 29–45, https://doi.org/10.1175/1520-0469(2000)057<0029:TIOCTF>2.0.CO;2.

Roberts, N. M., and H. W. Lean, 2008: Scale-selective verification of rainfall accumulations from high-resolution forecasts of convective events. *Mon. Wea. Rev.*, **136**, 78–97, https://doi.org/10.1175/2007MWR2123.1.

Rodwell, M. J., and Coauthors, 2013: Characteristics of occasional poor medium-range weather forecasts for Europe. *Bull. Amer. Meteor. Soc.*, **94**, 1393–1405, https://doi.org/10.1175/BAMS-D-12-00099.1.

Selz, T., and G. C. Craig, 2015: Upscale error growth in a high-resolution simulation of a summertime weather event over Europe. *Mon. Wea. Rev.*, **143**, 813–827, https://doi.org/10.1175/MWR-D-14-00140.1.

——, M. Riemer, and G. C. Craig, 2022: The transition from practical to intrinsic predictability of midlatitude weather. *J. Atmos. Sci.*, **79**, 2013–2030, https://doi.org/10.1175/JAS-D-21-0271.1.

Skamarock, W. C., 2004: Evaluating mesoscale NWP models using kinetic energy spectra. *Mon. Wea. Rev.*, **132**, 3019–3032, https://doi.org/10.1175/MWR2830.1.

——, and Coauthors, 2008: A description of the Advanced Research WRF version 3. NCAR Tech. Note NCAR/TN-475+STR, 113 pp., https://doi.org/10.5065/D68S4MVH.

Sun, Y. Q., and F. Zhang, 2016: Intrinsic versus practical limits of atmospheric predictability and the significance of the butterfly effect. *J. Atmos. Sci.*, **73**, 1419–1438, https://doi.org/10.1175/JAS-D-15-0142.1.

Tan, Z.-M., F. Zhang, R. Rotunno, and C. Snyder, 2004: Mesoscale predictability of moist baroclinic waves: Experiments with parameterized convection. *J. Atmos. Sci.*, **61**, 1794–1804, https://doi.org/10.1175/1520-0469(2004)061<1794:MPOMBW>2.0.CO;2.

Tribbia, J. J., and D. P. Baumhefner, 2004: Scale interactions and atmospheric predictability: An updated perspective. *Mon. Wea. Rev.*, **132**, 703–713, https://doi.org/10.1175/1520-0493(2004)132<0703:SIAAPA>2.0.CO;2.

Weyn, J. A., and D. R. Durran, 2019: The scale dependence of initial-condition sensitivities in simulations of convective systems over the southeastern United States. *Quart. J. Roy. Meteor. Soc.*, **145** (Suppl.), 57–74, https://doi.org/10.1002/qj.3367.

Zhang, F., N. Bei, R. Rotunno, C. Snyder, and C. C. Epifanio, 2007: Mesoscale predictability of moist baroclinic waves: Convection-permitting experiments and multistage error growth dynamics. *J. Atmos. Sci.*, **64**, 3579–3594, https://doi.org/10.1175/JAS4028.1.

——, Y. Q. Sun, L. Magnusson, R. Buizza, S.-J. Lin, J.-H. Chen, and K. Emanuel, 2019: What is the predictability limit of midlatitude weather? *J. Atmos. Sci.*, **76**, 1077–1091, https://doi.org/10.1175/JAS-D-18-0269.1.

Zhang, X., X.-Y. Huang, and N. Pan, 2013: Development of the upgraded tangent linear and adjoint of the Weather Research and Forecasting (WRF) Model. *J. Atmos. Oceanic Technol.*, **30**, 1180–1188, https://doi.org/10.1175/JTECH-D-12-00213.1.